Ultraviolet Photoacoustic Remote Sensing Microscopy

by

Nathaniel Haven

A thesis submitted in partial fulfillment of the requirements for the degree of

Master of Science

in

Biomedical Engineering

Department of Electrical and Computer Engineering
University of Alberta

© Nathaniel Haven, 2019

Abstract

Cancer is currently one of the leading causes of death globally. In dealing with certain cancers, the recommended treatment is often surgery. In order to determine if the entirety of the cancerous mass has been removed, tumor resection margins are assessed after surgical resection, as it is difficult to differentiate cancerous from health tissue without micro-scale observation. Presently, the current gold-standard for tissue biopsy and tumor resection margin analysis is formalin-fixed paraffin-embedded hematoxylin & eosin (H&E) histology. Though, this process is both time consuming and labor intensive as well as being a significant burden on the healthcare economy. Unfortunately, there are currently no intraoperative techniques capable of reproducing reliable post-operative H&E histology output, this results in many patients having to undergo secondary surgeries, leading to unnecessary emotional and physical trauma for patients, as well as higher risks of worsened prognosis. Here we report the development of an ultraviolet excitation photoacoustic remote sensing microscopy system capable of producing images of cell nuclei within cell cultures and tissue samples. This was achieved in two iterations. The first iteration utilized a parabolic focusing element along with mechanical stage scanning to obtain images of sectioned HT1080 CAM tumors, as well as HeLa cell cultures, demonstrating the ability to observe individual cell nuclei with good comparison

to H&E histology. However, the resolution of this system, determined to be 0.70-μm, could be improved and mechanical stage scanning resulted in slow acquisition speeds. In order to improve on these shortcomings, the second iteration moved towards a reflective objective focusing element, along with galvanometer optical scanning, able to clearly image cell nuclei in a variety of tissue samples with a determined resolution of 0.39-μm. The by-product of using a higher numerical aperture objective resulted in a tighter depth-of-focus, permitting the demonstration of superficial optical sectioning within tissue samples, where individual cell layers could be observed whilst rejecting background signal from cell layers outside the focal plane. In order to move closer towards an intraoperative translation goal, preliminary work was conducted in the direction of faster wide-field imaging with this system. This work showcased the widefield scanning abilities of focusing prior to optical scanning, as well as miniaturization capabilities using MEMS based optical scanners. Overall, the system presented has real potential to develop into a solution to the tumor resection margin analysis problem.

Preface

This thesis is original work by Nathaniel J. M. Haven. The research project, of which this thesis is a part, received research ethics approval from the University of Alberta Research Ethics Board, Project Name "Molecular Imaging with Photoacoustics and Ultrasound", AUP00001170, renewed 19th July 2019.

Some work in this thesis derives from collaboration with some current and previous lab members working under Dr. Zemp. Chapters 1, 2, 5 and 6 are original work done by Nathaniel J. M. Haven.

Chapter 3 has been published as: N. J. M. Haven, K. L. Bell, P. Kedarisetti, J. D. Lewis, and R. J. Zemp, "Ultraviolet photoacoustic remote sensing microscopy", Opt. Lett. 44, 3586-3589 (2019). I was responsible for designing and setting up the optical system, data collection, and manuscript writing. Kevan L. Bell helped set-up the optical system as well as helped with acquiring data. Pradyumna Kedarisetti was responsible for obtaining tissue and cell culture samples. John D. Lewis was the supervisory author whose lab resources were used for cell culture and tissue sample generation. Roger J. Zemp was the supervisory author involved with conceptual development and manuscript preparation and whose lab resources were used for optical set-up.

Chapter 4 contains work that has been recently submitted for publishing. I was responsible for designing and setting up the optical system, data collection, and manuscript writing. Pradyumna Kedarisetti was responsible for obtaining tissue and cell culture samples. Brendon Restall helped set-up the optical system as well as with acquiring data. Roger J. Zemp was the supervisory author involved with conceptual development and manuscript preparation and whose lab resources were used for optical set-up.

Acknowledgements

I gratefully acknowledge the funding support of the Natural Sciences and Engineering Research Council of Canada, the Canadian Institutes of Health Research, the Canadian Cancer Society, the Government of Alverta, and the University of Alberta.

To begin with, I would like to express my sincere gratitude to my supervisor, Dr. Roger Zemp, who helped make this journey both a rewarding and enjoyable one. It would also not be fitting to forget to thank both past and present colleagues who have all helped in various ways (listed in no particular order): Brendon Restall, Matthew Martell, Pradyumna Kedarisetti, Cory Rewcastle, David Egolf, Tarek Kaddoura, Min Choi, Dylan Ma, Mayara Nascimento, Mohammad Rahim, Mahyar Ghavami, Chris Ceroci, Mohammad Maadi, Afshin Kashani, Eric Dew, Daniel Mildenberger, Shalawny Miller, and Suellen Lamb.

I would like to also thank my supervisory committee and the staff from the Electrical and Computer Engineering and Faculty of Graduate Studies and Research departments for their support in completing my studies.

Last but not least, I would like to thank my family and friends for their unconditional support and encouragement, without whom I would not be where I am today. In particular, to my parents, who pushed me to be the best that I can be, and to my wife, for always supporting and putting up with me, even during tough times. Olive – thanks for always being a good girl.

Table of Contents

List of Figures

List of Symbols

Below is a list of frequently used symbols along with their general meaning to aid the reader.

- p_0 – Initial induced pressure
- Γ – Grüneisen parameter
- μ_a – Optical absorption coefficient
- Φ – Optical fluence
- μ_s – Scattering coefficient
- g – Anisotropy factor
- β – Thermal coefficient of volume expansion
- κ – Isothermal compressibility
- ρ – Mass density
- C_V – Specific heat capacity at constant volume
- v_s – Speed of sound
- p – Acoustic pressure
- C_p – Specific heat capacity at constant pressure
- H – Heating function
- $R_{L,AR}$ – Acoustic resolution photoacoustic microscopy lateral resolution
- NA_{ac} – Acoustic numerical aperture
- f_0 – Center frequency
- $R_{L,OR}$ – Optical resolution photoacoustic microscopy lateral resolution
- λ – Wavelength
- NA – Numerical aperture
- R_A – Axial resolution

- Δf – Transducer bandwidth

Glossary of Terms

Below is a list of frequently used terms along with their general meaning to aid the reader.

- CM – Confocal Microscopy
- CFM – Confocal Fluorescence Microscopy
- CRM – Confocal Reflectance Microscopy
- DC – Direct Current
- DOF – Depth of Focus
- FFPE – Formalin-Fixed Paraffin-Embedded
- FSA – Frozen-Section Analysis
- FWHM – Full Width at Half Maxima
- H&E – Hematoxylin and Eosin
- LSFM – Light Sheet Fluorescence Microscopy
- MEMS – Microelectromechanical Systems
- MPE – Maximum Permissible Exposure
- MUSE – Microscopy with Ultraviolet Surface Excitation
- NA – Numerical Aperture
- NLM – Non-linear Microscopy
- OCT – Optical Coherence Tomography
- OR-PAM – Optical Resolution Photoacoustic Microscopy
- PAM – Photoacoustic Microscopy
- PARS – Photoacoustic Remote Sensing
- SIM – Structured Illumination Microscopy
- SNR – Signal to Noise Ratio

- UV – Ultraviolet
- UV-PAM – Ultraviolet Photoacoustic Microscopy
- UV-PARS – Ultraviolet Photoacoustic Remote Sensing

Chapter 1

Introduction

1.1 Motivation

Since the advent of bright-field microscopy, formalin-fixed paraffin-embedded (FFPE) hematoxylin & eosin (H&E) histology has remained the gold-standard in tissue sample preparation for microscopic level evaluation. One major post-operative clinical application that utilizes this processing technique is tumor resection margin demarcation. Where the tumor resection margin is qualitatively defined as the region of apparently non-cancerous tissue surrounding the tumor. A positive tumor resection margin indicates the presence of residual cancer cells within this margin, which has a variable quantitative definition depending on the source from a 1- to 2-mm width [1]. In dealing with solid cancers, the recommended treatment is often tumor resection, where surgeons remove all cancerous tissue from the patient in order to diminish the risk of cancer recurrence. However, in doing so, the objective is to minimize the removal of healthy tissue, since organ dysfunctionality and negative aesthetic consequences for the patient can result from aggressive removal of tissue from a wide margin around the tumor [2]. Thus, there is a need to assess margins of a tumor after surgical removal from the patient to ensure no residual cancer cells are present. In order to analyze these margins, H&E histology is carried out on sections of the resected tissue and then imaged. It is challenging to differentiate tumor from normal tissue under gross-scale analysis, however, on micro-scale analysis cancer cells can be differentiated from healthy cells due to significant

morphological differences between them. As an example, cancer cells typically have enlarged nuclei, as well as an increase in nuclear density.

Currently, these resected tumor samples must be analyzed post-operatively due to how time-consuming and labor-intensive the FFPE H&E histology process is, taking from ~10-hours to a few days [3]. As a result, upon determination of positive margins, additional repeat surgeries are often needed. Such surgeries result in negative consequences such as contributing to a significant health-care economic burden, as well as causing unnecessary avoidable patient distress, both psychological and physical, and often result in a worse severity prognosis for patients. In breast conserving surgery used to treat breast cancer, as many as 20-40% lumpectomy patients require additional surgery due to positive resection margins [4]. Likewise, diffusely invasive brain cancers, such as grade 4 glioblastomas, see more than 85% of reoccurrences at the resection cavity margin, indicating incomplete resection [5]. Additionally, positive surgical margins occur in 2-13% of patients after partial nephrectomy surgery for pT1a renal cancer [6]. These are just some examples illustrating the widespread severity of this problem across different types of cancers.

Although a significant healthcare problem, there are currently very few intraoperative tools available for surgeons to assist them in tumor margin diagnosis. Thus, there is an urgent unmet need for improved intraoperative tools which can rapidly image tissue microstructure, ideally in fresh un-sectioned thick tissues, label-free, and with image quality comparable to traditional FFPE H&E histology. Such a technique could eventually help inform surgeons of margin status while the patient is still on the operating table, enabling complete removal of cancerous tissue without the need for follow-up surgeries.

Additionally, such a modality could also have potential applications in cell culture studies, where a non-contact label-free technique could have advantages over the use of fluorescent dyes and stains, where stain variability can be problematic, and longitudinal studies are more complicated to conduct due to the

requirement of performing staining protocols on samples, subsequently disrupting the cell cultures.

1.2 Key Contributions

The main goal of this thesis is to introduce a newly developed ultraviolet excitation photoacoustic remote sensing microscopy system. This system can produce photoacoustic images of cell nuclei within cell cultures and tissue samples label-free and non-contact.

The first contribution introduces our first iteration of this ultraviolet photoacoustic remote sensing microscopy system (Chapter 3). DNA/RNA absorption peaks occur around 266-nm, by using this wavelength as an excitation source, and taking advantage of the photoacoustic effect, we can probe local refractive index modulations with a separate detection beam, where these modulations occur due to high initial pressures resulting from the photoacoustic effect. We propose a new system architecture that can produce non-contact label-free mechanically stage scanned images of cell nuclei within cell cultures and tissues samples.

The second contribution introduces the second iteration of this system (Chapter 4), where a high numerical aperture reflective focusing objective is used along with galvanometer scanning to obtain high resolution optically scanned images of cell nuclei, with emphasis on thicker and fresh tissue imaging. This is carried out by taking advantage of inherent superficial optical sectioning capabilities resulting from a tight depth-of-focus due to our high numerical aperture objective.

The final contribution of this thesis presents two systems, the first capable of wide-field optical-scanning imaging, by using optical focusing prior to galvanometer scanning, and the second, showcasing preliminary work in moving towards a miniaturized scan head by using a 2-axis MEMS-mirror scanning element. Together, this work moves us towards fast wide-field photoacoustic

remote sensing microscopy with the purpose of laying the foundations for intraoperative application of our ultraviolet photoacoustic remote sensing microscopy system.

1.3 Layout of Thesis

This thesis is organized as follows: Chapter 2 will provide background on photoacoustic imaging, as well as other current methods for cell nuclei visualization with the intent of differentiating cancerous tissue from healthy tissue. Deficiencies and unmet needs of the various methods will also be covered.

Chapter 3 introduces the first iteration of our ultraviolet photoacoustic remote sensing microscopy system for cell nuclei visualization. This chapter has been published as N. J. M. Haven, K. L. Bell, P. Kedarisetti, J. D. Lewis, and R. J. Zemp, "Ultraviolet photoacoustic remote sensing microscopy", Opt. Lett. 44, 3586-3589 (2019).

Chapter 4 details the second iteration of our ultraviolet photoacoustic remote sensing microscopy system with focus on higher resolution imaging and optical scanning. This chapter has been submitted for publication.

Chapter 5 contains work on photoacoustic remote sensing microscopy using optical scanning after the focusing element in an attempt to increase the obtainable field-of-view, and also outlines work using a MEMS-scanning element to move towards miniaturization of the scanning head and also faster imaging capability.

Finally, Chapter 6 will serve as a conclusion of the work described in this thesis, highlighting future work that we hope can be achieved with the system introduced.

Chapter 2

Background

2.1 Photoacoustic Imaging

2.1.1 The Photoacoustic Effect

The photoacoustic effect was first described by Alexander G. Bell in 1880 and explains the phenomenon where acoustic waves are generated following light absorption in a sample [7]. Following the absorption of a short laser pulse, light is converted into heat and this in turn gives rise to thermoelastic expansion of the absorbing target, resulting in the generation of a pressure wave that propagates away from the absorber [8].

In order to better understand the relationship between the absorbed light and the resulting induced pressure, two important timescales, relating to the laser pulse, must first be addressed. The first timescale, thermal relaxation time, characterizes thermal diffusion within the medium. For a laser pulse shorter than this timescale, heat conduction will be negligible during the duration of the laser pulse. The second timescale, stress relaxation time, characterizes pressure propagation, and similarly to thermal relaxation time, for a laser pulse shorter than this timescale, stress propagation is also negligible during the laser pulse duration [9]. Wang et al. determined that the excitation pulse width should be <100-ns in order to guarantee stress confinement, where stress confinement is much more stringent than thermal confinement [10].

Thus, for a laser pulse that is in both thermal and stress confinement, that is, the laser pulse duration is shorter than both the thermal and stress relaxation

times, the fractional volume expansion of the absorber is also negligible which allows us to form the following expression for the induced initial pressure [11]:

$$p_0(r) = \Gamma \mu_a(r) \phi(r\,; \mu_a, \mu_s, g) \tag{2.1}$$

where $p_0(r)$ denotes the induced initial pressure at point r; $\Gamma = \frac{\beta}{\kappa \rho C_V}$ is the Grüneisen parameter, a dimensionless parameter that relates how well thermal energy is converted to pressure, and is defined by the thermal coefficient of volume expansion (β), the isothermal compressibility (κ), the mass density (ρ), and the specific heat capacity at constant volume (C_V); μ_a is the optical absorption coefficient; Φ is the optical fluence; μ_s is the scattering coefficient; and g is the anisotropy factor.

Under thermal confinement conditions, the following photoacoustic equation is obtained, which describes photoacoustic acoustic wave generation and propagation in an inviscid medium:

$$\left(\nabla^2 - \frac{1}{v_s^2}\frac{\partial^2}{\partial t^2}\right) p(\vec{r}, t) = -\frac{\beta}{C_P}\frac{\partial H(\vec{r}, t)}{\partial t} \tag{2.2}$$

where v_s is the speed of sound; $p(\vec{r}, t)$ denotes the acoustic pressure at location $\vec{r}$ and time t; C_p denotes the specific heat capacity at constant pressure; and $H(\vec{r}, t)$ is the heating function which describes how thermal energy is converted per unit volume and per unit time [9].

From Equation 2.1 we can see that the strength of the induced initial pressure is proportional to the optical absorption coefficient, if we note that the optical absorption coefficient is in turn dependent on the wavelength of light, this indicates that an induced pressure will only be generated if the target's optical absorption coefficient is large enough at that particular wavelength. In other words, taken together with Equation 2.2, and by using an ultrasound transducer to detect generated propagating acoustic waves, absorption-contrast images can

be obtained with high relative sensitivity within the optical depth of focus due to background-free detection by selecting a laser wavelength for which a target absorber holds a high affinity to. This forms the basis of the field of photoacoustic imaging.

2.1.2 Optical-Resolution Photoacoustic Microscopy

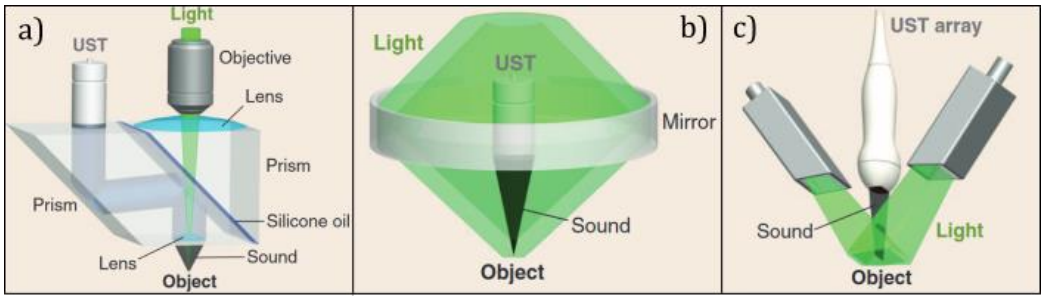

Figure 2.1: Typical PAT system architectures: a) OR-PAM; b) AR-PAM; c) Linear-array PACT. Reprint with permission from [12].

Photoacoustic tomography (PAT) can be divided into two main characterizations: photoacoustic computed tomography (PACT), and photoacoustic microscopy (PAM). As shown in Figure 2.1c PACT utilizes an array of unfocused ultrasound transducers to detect photoacoustic waves in parallel, requiring inverse reconstruction algorithms to reconstruct the tomographic image. Whereas PAM requires physical scanning of the acoustic and excitation focus across the sample [13].

Since PAM relies on optical excitation and ultrasound detection, the system can be further divided into Acoustic Resolution (AR-PAM), or Optical Resolution (OR-PAM). AR-PAM denotes a system in which the ultrasonic focus of the transducer detector is tighter than the excitation optical focus, as shown in Figure 2.1b. The lateral resolution of this system is directly proportional to the center frequency of the transducer, f_0, as well as the acoustic numerical aperture, NA_{ac}, and is given by Equation 2.3 [12].

$$R_{L,AR} = \frac{0.71 v_s}{NA_{ac} \cdot f_0} \tag{2.3}$$

Because the lateral resolution is directly related to the center frequency, by using a higher frequency transducer, the lateral resolution can be greatly increased. However, there is a trade-off that arises between lateral resolution and penetration depth, since ultrasonic scattering increases as a function of frequency to the fourth power. As an example, Zhang et al. achieved a 45-μm lateral resolution, with an imaging depth of 3-mm, using a transducer with $f_0 = 50$-MHz, and $NA = 0.44$ [14]. To achieve a 5-μm lateral resolution, $f_0 > 300$-MHz would be needed, at such high frequencies, the ultrasonic attenuation is on the order of ~80-dB/mm in tissue, which would limit the penetration depth to ~100-μm [15]. As a result, AR-PAM is typically used to achieve several micron to milli-order lateral resolutions at significantly deeper penetration depths than the transport mean-free path of the excitation wavelength, which is defined as the depth at which the direction of propagation of photons becomes randomized due to multiple scattering events, preventing tight focusing [16].

In contrast, OR-PAM, as shown in Figure 2.1a, has a lateral resolution determined by how well the excitation beam is focused, as shown in Equation 2.4, where λ denotes the wavelength of the excitation laser beam, and NA is the numerical aperture of the objective lens [12].

$$R_{L,OR} = 0.51 \cdot \frac{\lambda}{NA} \tag{2.4}$$

In contrast to AR-PAM, using OR-PAM architecture Zhang et al. were able to obtain a 220-nm lateral resolution, with an imaging depth of 100-μm using a 532-nm laser excitation beam and with $NA = 1.23$ [17]. However, since the resolution is defined by the optical excitation beam, penetration depth is limited by the transport mean free path of the excitation wavelength [18].

One parameter that both architectures have in common is the axial resolution. In photoacoustic imaging, the time of flight of ultrasound can then be used to characterize depth, and as a result, the axial resolution, denoted here as R_A, is determined by the bandwidth of the ultrasound transducer, Δf, as follows [12]:

$$R_A = 0.88 \cdot \frac{v_s}{\Delta f} \tag{2.5}$$

2.2 Photoacoustic Remote Sensing

2.2.1 Reflectivity Perturbation

One problem with photoacoustic imaging, is that since ultrasound waves must be detected, acoustic coupling between the receiving transducer and the sample is required. As a result, this modality is inherently contact based. This requires samples to be either submerged or to be in direct contact with an ultrasound transducer, either one of which could limit the application of this modality in certain use cases.

Recalling that a local initial pressure is generated after absorption induced thermoelastic expansion. From Equation 2.1, inserting typical values into the expression shows that these initial pressures can be very large (>MPa) [19]. It so happens that this initial pressure is large enough to result in a significant modulation of the existing refractive index, $n_0(r)$, of the target absorber by an amount $\delta n(r,t)$. This arises due to the elasto-optic effect which allows us to write the index of refraction as follows [19]:

$$n(r,t) = n_0(r) + \delta n(r,t) = n_0(r)\left(1 + \frac{\eta \mathrm{n}_0(r)^2 p(r,t)}{2\rho v_s^2}\right) \tag{2.6}$$

where η is the elasto-optic coefficient; $p(r,t)$ is the pressure field; ρ is the mass density; v_s is the speed of sound in the medium; and $n(r,t)$ is the resulting modulated refractive index.

Other than the elasto-optic modulation of the refractive index, thermal effects should also be considered since the refractive index is temperature dependent. However, in comparison, this has been found to be negligible due to slow temperature cooling [19].

For a refractive index modulation near a boundary, such that pressure loss in the acoustic wave is negligible, a strong modulation of the reflectivity can occur at the interface. For an absorbing medium with refractive index n_1, modulated by an initial pressure, and non-absorbing medium refractive index n_2, then the reflectivity coefficient change at normal incidence can be given by [19]:

$$\Delta R = \left|\frac{n_1 + \delta n - n_2}{n_1 + \delta n + n_2}\right|^2 - R \tag{2.7}$$

where R is the unperturbed reflectivity coefficient; and ΔR is the perturbation due to the photoacoustic initial pressure.

If we assume that δn is real, then we obtain the following expression [19]:

$$\Delta R = \delta n \left(\frac{2Re\{n_1 - n_2\}}{|n_1 + n_2|^2} - \frac{2Re\{n_1 + n_2\}}{|n_1 + n_2|^2}\left|\frac{n_1 - n_2}{n_1 + n_2}\right|^2\right) + \mathcal{O}(\delta n^2) \tag{2.8}$$

where $\mathcal{O}(\delta n^2)$ represents terms dependent on higher orders of δn. When the refractive indices are primarily real, then we can obtain the following relationship [19]:

$$\Delta R \propto \delta n(n_1 - n_2) \tag{2.9}$$

Equation 2.9 demonstrates that there is a linear relationship between the reflectivity perturbation and the index of refraction modulation. Remembering that Equation 2.6 showed dependency of the index of refraction modulation to the initial pressure, and that Equation 2.1 showed dependency of the initial pressure to the absorption coefficient, we are thus able to perform absorption-contrast imaging by measuring this reflectivity perturbation at the instant when these high initial pressures are induced.

2.2.2 Remote Sensing of the Reflectivity Perturbation

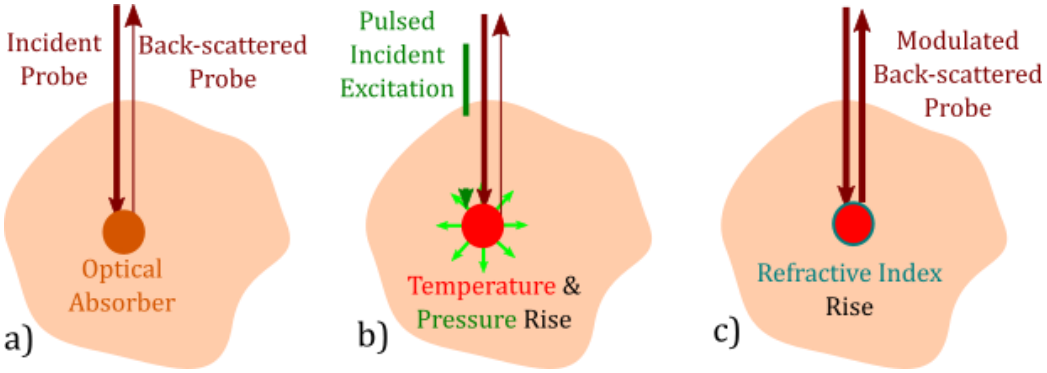

Figure 2.2: PARS mechanism: a) no incident excitation results in weak back-scattered probe beam; b) incident pulsed excitation generates temperature and pressure rise; c) resulting refractive index rise then modulates the back-scattered probe beam.

As shown in Figure 2.2, this reflectivity perturbation can be measured by including an additional continuous wave interrogation beam that is co-focused and co-aligned with the pulsed excitation beam. By measuring the modulation in the backscattered interrogation beam after each subsequent excitation pulse, a photoacoustic image can be obtained. However, in comparison to photoacoustic imaging, since there is no reliance on acoustic wave detection, this modality is non-contact, as well as being all-optical. This could have advantages in imaging

scenarios where physical contact is not desirable, and also in co-integration into existing all-optical imaging systems for multi-modal imaging.

Similarly to other ultrasound detection based photoacoustic imaging modalities, absorption contrast images are obtained label-free, where endogenous contrast is often targeted. Some examples of typically targeted endogenous contrast agents include oxy- and deoxy-hemoglobin, lipids, and melanin to name a few. Exogenous contrast agents can also be targeted, where organic dyes, nanoparticles, fluorescent proteins and report gene products have all been reported in literature [16].

Figure 2.3 displays images recently obtained using PARS microscopy. Figure 2.3b shows *in vivo* mouse ear vasculature imaged using 532-nm wavelength excitation, targeting hemoglobin, which represents the most abundant protein in blood, blood cells can also be observed in Figure 2.3d [20]. Furthermore, by taking measurements at two wavelengths, the relative concentrations of oxy- and deoxy-hemoglobin can be quantified, and thus oxygen saturation (sO_2) can be computed, as shown in Figure 2.3a [20]. Since PARS requires both an excitation and detection beam, the lateral resolution of the system is dependent on which beam has a tighter focus. As a result, by using a loose excitation focus, the lateral resolution can be determined by the detection beam. This is advantageous because a higher wavelength detection beam can then be used, where the transport mean-free path of the detection beam is significantly larger than that of the excitation beam, allowing for much deeper imaging. Figure 2.3c shows this in action, where vasculature could be imaged up to depths of 1.2-mm *in vivo* using a 1319-nm detection beam [21].

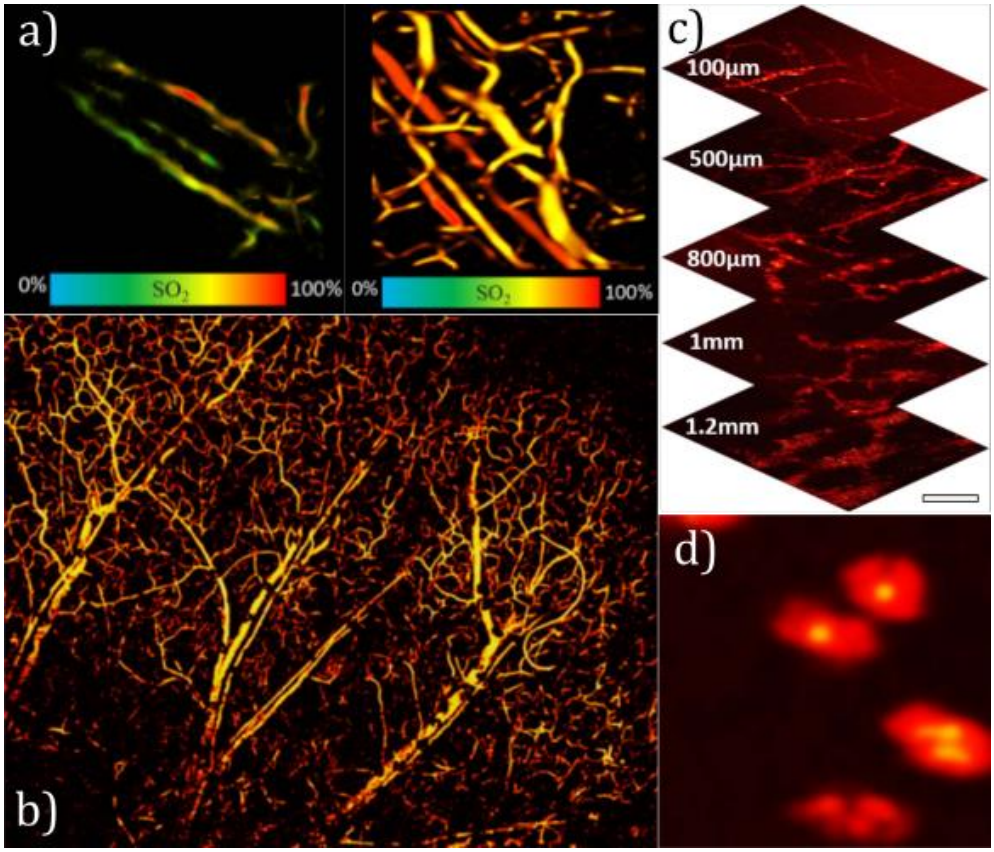

Figure 2.3: PARS microscopy images of mouse ear vasculature: a) *in vivo* results of sO_2 unmixing; b) wide-field image; c) image taken at various depths using deep-penetrating mode, scale bar: 100-µm width; d) image of individual red blood cells. Reprint with permission from [20] (a, b, d), and [21] (c).

2.3 Standard Histopathology

2.3.1 Formalin Fixed, Paraffin Embedded (FFPE) Hematoxylin and Eosin (H&E) Histology

FFPE H&E histology is the current gold standard in evaluating surgical margins. Steps in this process involve first grossly "bread-loafing" tissue into ~2-mm to 1-cm thick serial slices [22], then tissue fixation, followed by dehydration (typically using alcohol and xylene), paraffin embedding, sectioning via microtomy (typically 4-μm thick), rehydration, and then staining with H&E [23]. Where hematoxylin stains the nucleus of cells purplish blue, and eosin stains the cytoplasm red. While much of this is automated, it is still time-consuming, taking around ~10-hours to a few days, and is labor intensive, requiring input from highly skilled technicians [3]. The labor intensive, time consuming processing results in a high required overhead for equipment, consumables, and labor, all resulting in a cost ineffective method.

In addition, interpretation can be subjective as a result of sampling errors due to only being able to section a sparse 10-15% of the tissue surface [1], in which <1% of the surgical margin surface is visualized [4], as well as process induced distortion artifacts resulting in the loss of some biological components. Moreover, the destructive nature of routine FFPE H&E histology compromises the value of tissues for further analysis downstream. Additionally, stain variability, where variations in the color and intensity of H&E stained samples occur, can also result in ambiguous results [24]. This stain variability often occurs due to the vast number of procedures currently in operation, with more than 4,500 processes, making up 95% of processes, developed principally between 1841 and 1950 [25]. Although, certain studies such as work by Bejnordi et al. have looked into standardizing stain intensity and color using automated algorithms [24].

2.3.2 Frozen Section Analysis (FSA)

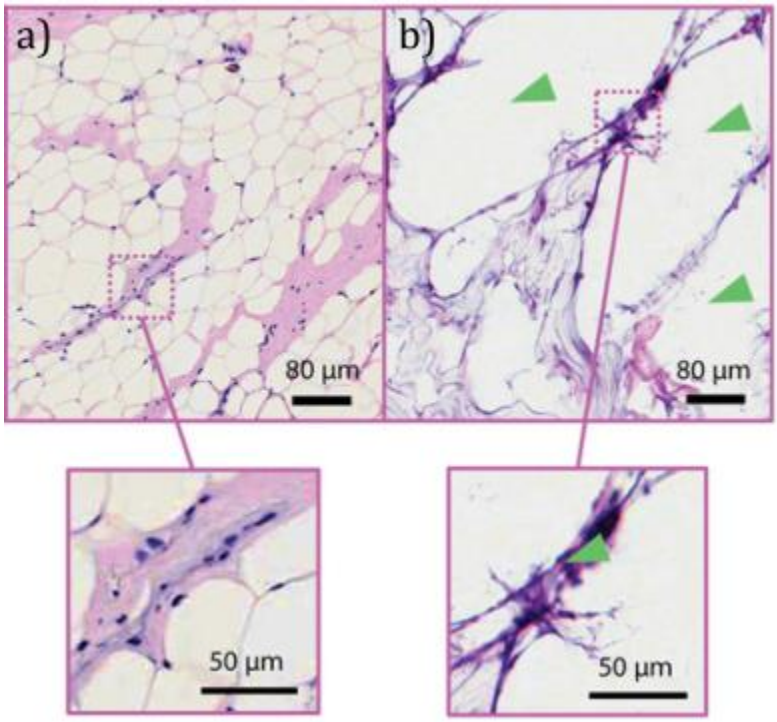

Figure 2.4: Intraoperative microscopy of fresh human breast fibro-adipose tissue: a) conventional FFPE H&E histology image; b) frozen tissue section H&E histology image. Reprint with permission from [30].

FSA is often used as an intraoperative alternative to conventional FFPE H&E histology, however, has not been widely accepted as part of standard of care due to certain limitations. It requires embedding tissue within optimal cutting temperature compound, followed by freezing, sectioning with a cryostat and H&E staining [26]. Compared to FFPE H&E histology, FSA is likewise labor-intensive, however, offers much faster processing times, at around ~20-30-mins per section. Nevertheless, evaluation of multiple frozen sections takes too long for intraoperative analysis, significantly increasing surgery time [1]. Like FFPE H&E histology, FSA suffers from under-sampling of the resected tumor specimen

surface, where under-sampling is often more severe due to time constraints in an intraoperative setting versus a post-operative setting. Additionally, FSA requires destructive removal of tissues that should ideally be preserved for FFPE H&E post-operative histology. It has also been shown to have reduced accuracy in multiple studies, McLaughlin et al. found that FSA indicated false positive results in 44% of cases for sentinel lymph node analysis [27], whereas, Eberlin et al. found that FSA results were unreliable in up to 30% of patients undergoing resection of gastrointestinal cancers [28]. Moreover, it is especially challenging in adipose tissues, where freezing artifacts are more likely to occur and there are difficulties in physical sectioning [29]. Figure 2.4 illustrates freezing artifacts that can occur, where it is clear that in Figure 2.4b fibro-adipose tissue has degraded considerably compared to the FFPE H&E histology shown in Figure 2.4a.

2.4 Alternative Approaches

Aside from FSA, a number of other approaches have been proposed to try to replace the conventional FFPE H&E histology gold standard. To begin with we briefly discuss a broad range of reported alternative approaches, which seek to differentiate cancerous from normal tissue on the macro-scale. We then follow this discussion with a lengthier description of some of the main alternatives that compete directly with our technique reported in this thesis, that is, seek to produce micro-scale histopathology-like output. The list of alternatives is by no means exhaustive, but rather should give the reader a measure of the broad range of techniques currently available, where their respective advantages and disadvantages are also addressed.

Touch preparation cytology is a technique currently used intraoperatively in some clinics that relies on the detachment of cancers cells from the surface of a resected tumor specimen as a glass slide is pressed to the surface with the dependence on these cells adhering to the slide for imaging. This allows the entire surface of the specimen, albeit only the superficial layer, to be imaged. The

restriction to only superficial layers, thus renders this technique unable to determine resection margins [31].

Fluorescence-guided tumor resection uses administered fluorescent dyes to aid surgeons in gross tumor demarcation during tumor resection surgery. This has been successfully used in intraoperative studies with a variety of dyes. However, limitations include poor tissue specificity, with some dyes leaking to surrounding tissues, as well as many of the available dyes not being approved by the Food and Drug Administration [32].

Desorption electrospray ionization mass spectrometric imaging has recently shown promise in assessing surgical resection margins. Samples are bombarded with microdroplets, resulting in the emission of secondary microdroplets, containing dissolved chemicals from the sample, that enter a mass spectrometer. This generates a detailed map of the distribution of molecules within the sample surface, whilst resulting in low tissue damage. Limitations of this technique include poor resolution, on the order of 200-μm, as well as relatively slow acquisition times per sample point, at 0.5-s/pixel [27].

Other techniques worth mentioning, that provide macro-scale contrast, include radiofrequency spectroscopy [33], diffuse reflectance spectroscopy [34], ultrasound-guided surgery [35], terahertz reflectometry [36], micro-computed tomography [37], and magnetic resonance imaging guided surgery [38]. Phase-contrast microscopy is also a noteworthy micro-scale contrast imaging modality [39].

2.4.1 Microscopy with Ultraviolet Surface Excitation (MUSE)

MUSE relies on two important characteristics. Firstly, that UV light at wavelengths shorter than 300-nm only penetrates a few microns into tissue, thus effectively resulting in superficial optical sectioning and secondly, that this wavelength range generates strong visible light emission from tissue specimens stained with conventional fluorescent dyes.

The tissue specimen is illuminated by oblique UV excitation light from a light-emitting diode that passes through a UV transparent window, this light bypasses an objective lens that collects the visible fluorescent emission which is then focused onto a camera. Fereidouni et al. used 280-nm excitation along with a range of dyes including rhodamine and Hoechst [23]. Using this combination, MUSE is able to obtain impressive histopathology images of both fresh and fixed un-sectioned tissues that can be stained very quickly as shown in Figure 2.5a, and b, displaying the color converted virtual H&E MUSE image, compared to Figure 2.5c showing the conventional FFPE H&E stained image. However, due to optical sectioning capability being reliant on UV penetration depth, which is slightly greater than the thickness of a typical tissue section, has trouble differentiating single cell layers. Since UV penetration depth is tissue dependent, image contrast, which depends on optical sectioning capability, is likely to vary depending on regions of tissue being imaged. Additionally, this mechanism in which optical sectioning is obtained results in a limited ability to perform any type of volumetric imaging. Work by Xie et al. next moved MUSE towards intraoperative imaging of breast tissue surgical margins, with the ability to label fresh tissue within ~5-mins. Good comparisons were made to FFPE H&E stained samples, however, the optical sectioning thickness of MUSE, determined to be on the order of 10 to 20-μm, significantly greater than 4-μm histology sections, as well as

MUSE imaging deformable un-sectioned tissue versus rigidly embedded sectioned tissue resulted in some disparities between the two modalities [40].

One additional potential problem with intraoperative translation of MUSE is a result of tissue auto-fluorescence, and additional signal from fluorescence dyes, which results in produced images that contain a lot more extra information than conventional H&E stained images that is challenging to isolate, this could have the negative impact of resulting in confusion when analyzed by pathologists [23].

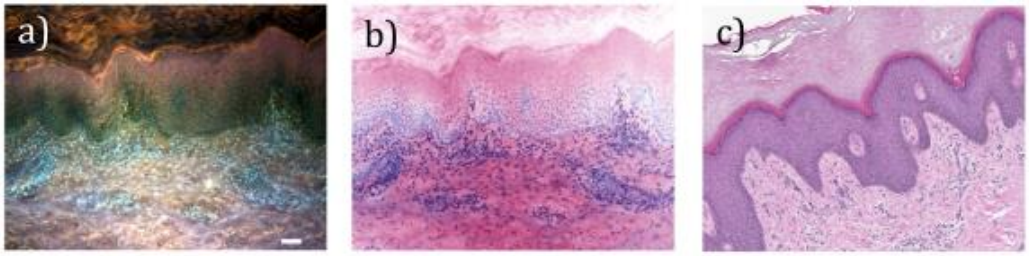

Figure 2.5: Sample images from a validation study: a) MUSE image stained with rhodamine and Hoechst; b) Colour converted virtual H&E MUSE image; c) Conventional FFPE H&E histology image, scale bar: 100-µm width. Reprint with permission from [23].

2.4.2 Optical Coherence Tomography (OCT)

In OCT a broadband source is used, since the axial resolution is directly proportional to the coherence length, which is inversely proportional to the bandwidth, and this source is split between two arms, the reference arm, and the sample arm. The sample arm focuses the light onto the sample and then the back-reflection is fed back to a detector. Similarly, the reference arm is terminated by a mirror and this back-reflection is also fed back to the same detector. Due to the low coherence length of the source, broadband interference between the reference and sample back-reflected light is only observed when the optical pathlengths differ by less than the coherence length of the light source. It turns however, that this broadband interference contains depth information. Thus, in

Spectral-domain OCT, by spectrally separating and recording this broadband interference using e.g. a grating within a spectrometer, and then taking a Fourier Transform of this data, optical reflectivity versus depth information can be obtained [41].

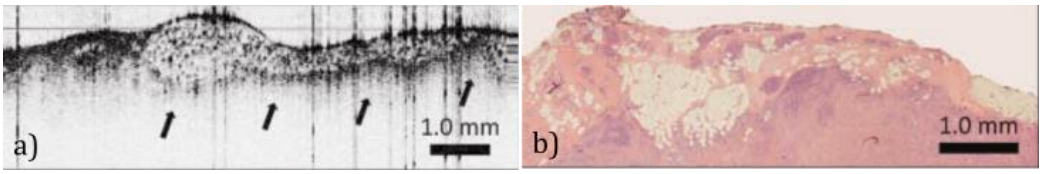

Figure 2.6: Breast tumor margin imaging: a) image taken using OCT, arrows indicates highly scattering foci indicative of collections of tumor cells; b) FFPE H&E histology image. Reprint with permission from [1].

Nguyen et al. designed a spectral-domain OCT system employing a 1310-nm superluminescent diode with 92-nm bandwidth, resulting in an axial resolution of 5.9-μm, and lateral resolution of 35-μm, with the capability to image sub-surface depths up to 2-mm. Breast lumpectomy samples were imaged with this modality with limited success, where certain features showed agreement with FFPE H&E histology. However, the obtained images lacked the level of detail found in these histology sections as shown in Figure 2.6 [1]. Other work by Erickson-Bhatt et al. took this a step further by imaging *in vivo* resection beds [42]. Nevertheless, being a scattering imaging modality, key limitations that present themselves are an inherent inability to provide strong contrast to cell nuclei due to typically very small refractive index differences of subcellular structures, which is further constrained in highly scattering tissues. Furthermore, OCT is not conventionally designed for subcellular resolution, typically using longer probing wavelengths and low NA focusing. However, being a wide-spread imaging modality it has the advantage of availability, as well as being label-free.

2.4.3 Confocal Fluorescence/Reflectance Microscopy (CFM/CRM)

Conventional wide-field fluorescence microscopy uniformly illuminates the entire field-of-view with excitation light. This however, results in fluorescence emission from fluorophores outside the plane of focus, generating a significant amount of background fluorescence signal. This unwanted background signal degrades contrast of features located in the focal plane. In comparison to conventional microscopy, where widefield illumination is used, CFM uses focused illumination, where fluorescence emission is then further spatially filtered using a pinhole to reject emission from outside the focal plane. This results in the ability to optically section thick specimens by only illuminating small volumes of fluorophores and rejecting any remaining background fluorescence. However, as a result of requiring focused illumination, point scanning is required to obtain a full image, leading to significantly longer image acquisition times compared to wide-field illumination microscopy [43].

Ragazzi et al. used a CFM system in order to image cell nuclei in a variety of tissue types stained with acridine orange, which binds to nucleic acids and in particular DNA. Overall, good comparisons could be made to conventional FFPE H&E histology images, however, in some tissue types, such as in the Lymph node, high nuclear density in some regions resulted in strong fluorescence emission where individual cell nuclei could not be made out [44]. Furthermore, the requirement for fluorescence dyes could result in stain variability.

Alternatively, CRM, like the previously described OCT, relies on scattering contrast rather than fluorescence contrast, while maintaining the optical sectioning capability of the confocal microscopy architecture. Eschbacher et al. used CRM to image brain tissue samples, as shown in Figure 2.7, where the corresponding colorized image in Figure 2.7b shows an ability to obtain contrast between cell nuclei and surrounding cytoplasm. However, although promising,

this contrast was very dependent on the types of tissue, with more highly scattering tissue giving much poorer scattering contrast [26]. To add to this, the inherent inability to reject background scattering signal due to low specificity to nuclei contrast, results in images that require more training to interpret compared to conventional FFPE H&E histology images, limiting the ability to translate CRM into an intraoperative setting.

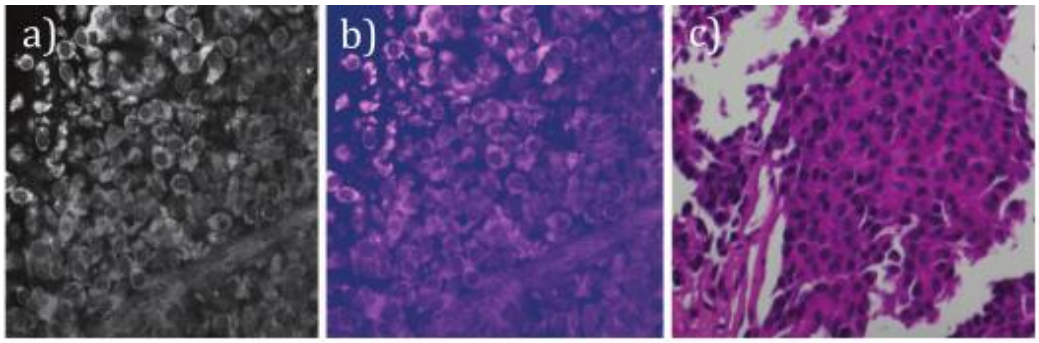

Figure 2.7: Human brain pituitary adenoma imaging: a) confocal reflectance microscopy image; b) correspond colorized look-up table image of a); c) frozen section H&E histology image. Reprint with permission from [26].

2.4.4 Non-linear Microscopy (NLM)

NLM includes two-photon autofluorescence (2PAF), three-photon autofluorescence (3PAF), second-harmonic generation (SHG), third-harmonic generation (THG), coherent anti-Stokes Raman scattering (CARS), and stimulated Raman scattering (SRS), all of which can be employed both label-free, where in the case of multi-photon microscopy, intrinsic autofluorescence is targeted rather than exogenous fluorescence dyes. 2PAF and 3PAF involve the near-simultaneous absorption of two photons and three photons respectively, resulting in an excitation approximately equal to that of a single photon of double or triple the energy respectively. The first photon generates a virtual state of the electron, and the proceeding photons must be absorbed before this state is de-excited. One interesting feature of 2PAF and 3PAF is that excitation has a

quadratic and cubic dependence on intensity respectively. This has the consequence of much tighter optical sectioning, as well as lower photobleaching due to a smaller excitation volume [45].

SHG and THG involve the sum frequency doubling and tripling to produce emission at twice and triple the energy of the excitation light respectively. These harmonic wavelengths emissions are not usually absorbed and are instead directly detected signifying the presence of certain media properties required for the SHG and THG processes, this factor reduces phototoxicity compared to other excitation processes. Like 2PAF and 3PAF, SHG and THG emission also has a quadratic and cubic dependence on intensity respectively, again resulting in tight optical sectioning [45].

CARS describes the four-wave mixing process in which a pump and Stokes photon with frequencies ω_p and ω_S respectively excite a vibrational level at an energy $\hbar(\omega_p - \omega_S)$. A third probe photon at ω_p' then interacts with the excited level to emit a single photon at the anti-Stokes frequency of $(\omega_p - \omega_S + \omega_p')$. Vibrational contrast in CARS microscopy is obtained when $\omega_p - \omega_S$ is tuned to a Raman-active vibrational band. Since the vibrational band is excited using a difference in frequencies this means visible wavelengths can be used rather than traditional infrared excitation. The resulting CARS signal has a quadratic dependence with respect to the pump intensity and linear dependence on to the Stokes intensity, thus resulting in tight optical sectioning [46, 47]. Compared to CARS, SRS is a further development only requiring two frequencies, the pump and Stokes frequencies, ω_p and ω_S. Similar to CARS, the Raman shift, $(\omega_p - \omega_s)$, is selected to match a particular vibrational level, which results in resonance and a resulting amplified Stokes intensity and corresponding pump intensity loss, these can then be measured. Unlike CARS, this only occurs when a particular vibrational level is matched, thus SRS does not exhibit non-resonant background signal, resulting in almost background-free imaging contrast. Like CARS, SRS can also achieve tight optical sectioning due to its non-linear dependence on the pump and Stokes intensity [48].

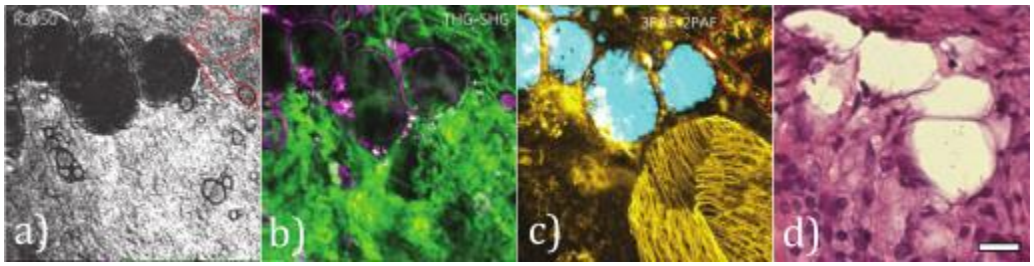

Figure 2.8: Rat mammary tumor specimen imaging: a) CARS image at R3050 peak; b) joint THG-SHG image, THG is shown in magenta, and SHG shown in green; c) joint 3PAF-2PAF image, 3PAF is shown in blue, and 2PAF shown in yellow; d) FFPE H&E histology image, scale bar: 30-μm width. Reprint with permission from [3].

Tu et al. designed a multimodal system based on a novel widely coherent supercontinuum photonic-crystal fiber source to obtain 2PAF, 3PAF, SHG, THG, CARS, and SRS based images. Figure 2.8a shows the CARS response at 3,050-cm^{-1}, corresponding to protein/water contrast, identified predominantly in stromal regions, a response at 2,850-cm^{-1} was also obtained which corresponds to lipid contrast. Figure 2.8b shows a joint THG-SHG image, where the THG response is due to optical heterogeneity, typically giving lipid contrast and SHG response is due to noncentrosymmetry, typically giving collagen contrast. Figure 2.8c shows a joint 3PAF-2PAF image, where the 3PAF response is due to nicotinamide adenine dinucleotide (NADH) autofluorescence, and 2PAF is due to flavin adenine dinucleotide (FAD) autofluorescence [3]. Overall, this broad range of contrast mechanisms provide a lot of histochemical and structural specimen information. However, this contrast can be more difficult to directly translate into a comparable conventional H&E image, especially since direct DNA contrast is not generally accessible, rather, an absence of signal is usually used to locate nuclei.

Similar to this system, another multimodal system named simultaneous label-free autofluorescence—multiharmonic microscopy (SLAM) was recently introduced by You et al. This modality obtains SHG, THG, 2PAF, and 3PAF based

images using a single-excitation band and has produced impressive images of tumor microenvironment in a living rat [49]. The advantage of this system is that it only requires a single laser and can simultaneously record contrast from the mechanisms mentioned above. However, despite this, the expensive ultrafast lasers required to obtain contrast from these mechanisms is the biggest disadvantage of NLM. Furthermore, due to inherent tight optical sectioning, limitations are placed on optical scanning, resulting in long image acquisition times, restricting the extent to which this could be translated into an intraoperative setting.

2.4.5 Light Sheet Fluorescence Microscopy (LSFM)

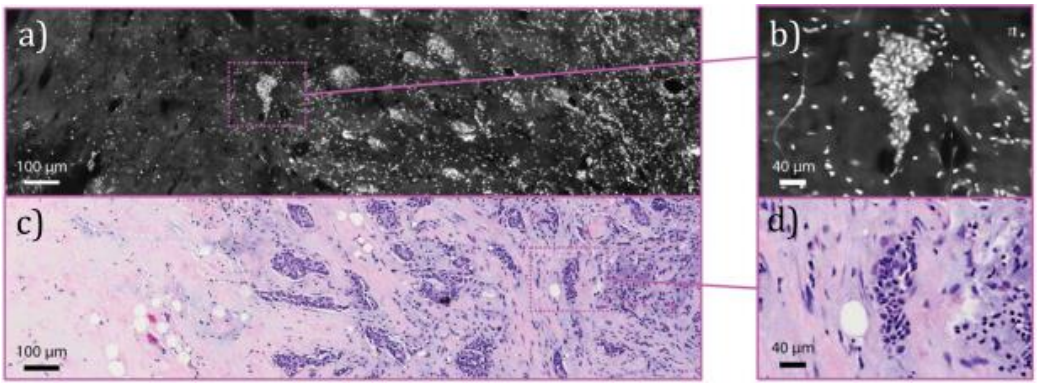

Figure 2.9: Intraoperative microscopy of fresh human breast fibro-adipose tissue: a) LSFM image; b) magnified view of dotted box in a); c) conventional FFPE H&E histology image; d) magnified view of dotted box in c). Reprint with permission from [30].

LSFM uses light sheet illumination to generate fluorescence, where either a thin static generated light sheet or dynamically formed light sheet is used. The illumination and detection pathways are separated such that detection is usually carried out orthogonal to the illumination, and the detected light is collected using an objective which determines the lateral resolution of the system. The axial resolution, and optical sectioning capability, is determined by the thickness

of the light sheet. Generally, since the de-coupled illumination and detection pathway positions are aligned to each other, rather than typical illumination beam scanning, the sample is instead scanned [4].

Glaser et al. recently reported an open-top LSFM system, where the sample is placed on top of a glass slide and index-matching optics are used to reduce severe aberration effects due to highly off-axis illumination and collection. After illumination, oblique fluorescence emission sheets are collected by an objective and fed to a camera, and the sample is then stage-scanned to allow for imaging of serial oblique light sheets, producing a 3D trapezoidal volume that can be quickly imaged. Using this approach rapid intraoperative assessment of breast tissue stained with acridine orange for only 20 seconds was achieved showing good agreement to standard H&E stained samples as shown in Figure 2.9, where invasive ductal carcinoma can we seen with adjacent normal breast tissue [30]. Advantages of this modality are that it can obtain 2D oblique light sheets directly, allowing for rapid 3D microscopy. Furthermore, a de-coupled detection and illumination path allows each path to be optimized independently. An extended depth of focus also helps to accommodate for tissue-surface irregularities. However, can be costly due to the requirement of a sensitive high-speed camera as well as a high-quality collection objective, and often requires the use of optical clearing agents. Additionally, this modality requires the use of fluorescence dyes, some of which can be slow acting especially in thicker tissue samples, as well as can lead to staining variability.

2.4.6 Structured Illumination Microscopy (SIM)

SIM uses widefield illumination with a specifically defined spatial pattern. This spatial pattern is imparted onto the beam using a spatial light modulator, where generally a sinusoidal pattern is used. The result of this is that, through the use of a demodulation algorithm on the detected fluorescence signal, emitted fluorescence from outside the focal plane can be rejected after collection by a

camera. The axial resolution, and thus optical sectioning thickness, can be tuned by changing the spatial frequency of the sinusoidal pattern. This spatial frequency can also be increased to improve axial resolution up to a certain point [50].

Fu et al. designed a SIM system with a reported 4.4-µm lateral resolution and were able to obtain images with good comparison to standard H&E stained images, with significantly greater contrast compared to uniform widefield illumination [51]. Other work in this area by Wang et al. was also able to achieve circumferential surface imaging of fully intact prostates, with imaging speeds approaching that required for intraoperative translation. Figure 2.10 shows the quality of image obtained with this system [50].

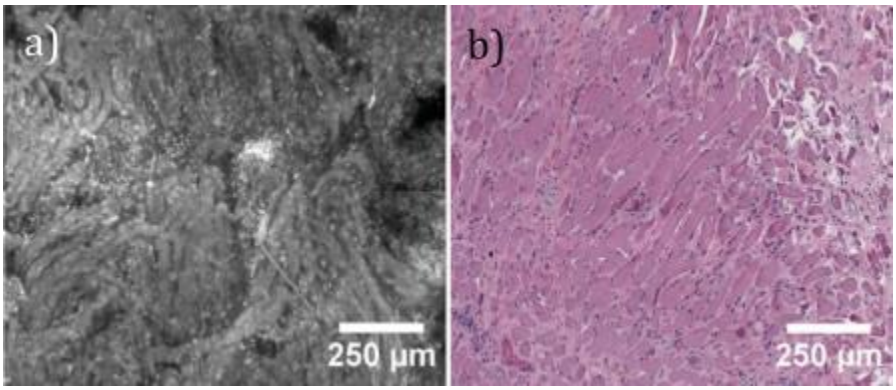

Figure 2.10: Clinical image of normal skeletal muscle of prostate tissue: a) SIM image; b) conventional FFPE H&E histology image. Reprint with permission from [50].

SIM has shown great potential for fast histology-like imaging especially in the case of superficial imaging of large areas of tissue and appears to be close to translation within an intraoperative setting. However, the modality still suffers from a number of limitations, it is limited to surface imaging for most tissues with reduced performance in deep imaging. The requirement of a spatial light modulator, as well as a high-speed camera can be expensive. Furthermore, an issue can arise with rejecting out of focus background post-capture, in that for thicker samples out of focus background can occupy the majority of the camera

dynamic range leaving a small fraction for the in focus signal, coupled with shot noise from this background, it becomes difficult to achieve high signal to noise ratios [52].

2.4.7 Ultraviolet OR-PAM (UV-PAM)

Recently, Yao et al. determined that DNA and RNA, which are two major components of cell nuclei, strongly absorb wavelengths within the 245 and 275-nm range. They also concluded that this wavelength range could be used for PAM imaging of cell nuclei with high optical contrast, where absorption of protein and lipids is weaker by 1 order of magnitude at 260-nm [53]. Following from this, they then went on to showcase the first *in vivo* label-free OR-PAM images of cell nuclei, achieved using a 266-nm 7-ns pulse width laser, along with a ring-shaped focused transducer with 50-MHz center frequency and 7-mm focal length. The laser pulse energy behind the membrane (imaging window) was measured to be 35-nJ. Lateral and axial resolutions of 0.70±0.04-μm and 28.5±0.8-μm were obtained respectively [54]. Images were taken of a cross-section of a mouse small intestine, where good agreement could be seen between H&E stained images and the images taken with the UV-PAM system.

In order to improve on this lateral resolution, Wong et al. developed a transmission-mode UV-PAM architecture, which boasted an impressive ~0.33-μm lateral resolution, able to obtain good comparisons to conventional FFPE H&E histology images of breast tissue as shown in Figure 2.11. Although interestingly, Figure 2.11e and f illustrate situations where densely packed nuclei, as found within ducts, can be seen in the conventional histology image, but not in the UV-PAM image, where instead a bright dense feature is seen. One limitation of this system is that due to being transmission-mode, this architecture is not suitable for imaging of thick tissues, highlighting a problem with UV-PAM systems in which the requirement for acoustic detection necessitates partially distinct optical and acoustic paths, resulting in a constraint on operational

numerical apertures. Thus, for thick tissue imaging, which requires reflection-mode operation, it is not currently possible to obtain high lateral resolutions with UV-PAM systems. Moreover, this system had an axial resolution of ~48-µm, resulting in poor optical-sectioning and subsequent detection of signal from multiple cell layers [55].

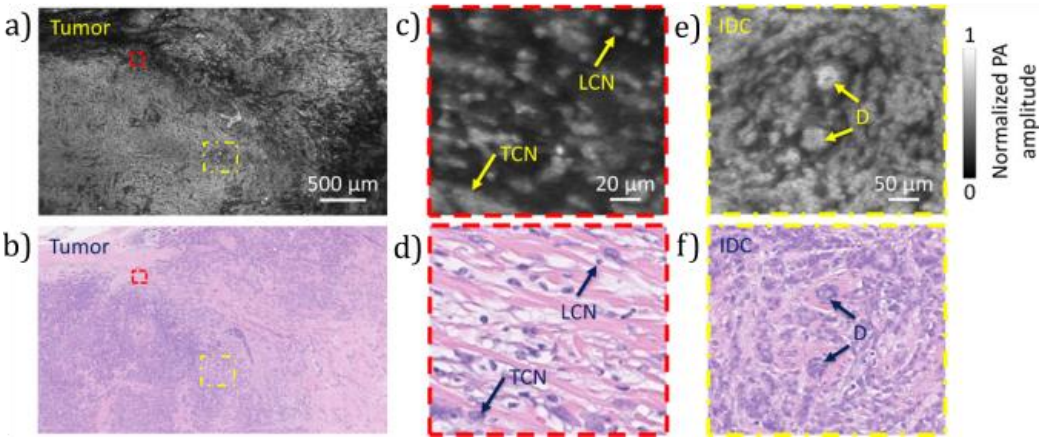

Figure 2.11: Imaging of breast tumor: a) UV-PAM image; b) conventional FFPE H&E histology image; c) and d) zoomed-in UV-PAM and H&E histology images of red dashed regions in a) and b) respectively; e) and f) zoomed-in UV-PAM and H&E histology images of the yellow dashed regions in a) and b) respectively. TCN, tumor cell nucleus; LCN, lymphocyte cell nucleus; IDC, invasive ductal carcinoma; D, duct. Reprint with permission from [55].

Two recent methods have been proposed to improve this axial resolution, the first by Cai et al. involves using two excitation beams instead of one, where these are orientated orthogonal to each other, using this technique an axial resolution improvement from ~37-µm to ~1.8-µm was achieved [56]. Another method by Lie et al. exploited the Grüneisen relaxation effect. Where the Grüneisen parameter can be altered by transient light absorption and then relaxed to its baseline value over time. In brief, a pre-heating laser pulse was fired before the main photoacoustic excitation pulse, resulting in an increase in the Grüneisen parameter. This results in a photoacoustic signal that is no longer invariant with depth, instead decaying as absorbers are axially moved away from the optical

focus – thus resulting in optical sectioning. Using this method they were able to achieve a 15-μm axial resolution compared to the acoustic axial resolution of ~48-μm [57].

One other limitation so far is that these systems have relied on slow mechanical scanning, which limits the ability to translate this modality into an intraoperative setting. To move closer towards this goal, Imai et al. developed a UV-PAM system that uses a microlens array of 40 lenses. A lateral resolution of ~1.6-μm was reported, with a 40x decrease in imaging scanning time compared to point-by-point scanning. In theory the microlens density is limited by the acoustically determined lateral resolution of the 1-D array transducer, determined to be 75-μm, if the microlens spacing approaches this value, overlap would begin to occur, increasing crosstalk. By increasing the microlens array density, the imaging speed can be increased proportionally. The main limitations that arise from this method of illumination is that the laser power is distributed between all microlenses, so to have a high enough microlens density with sufficient pulse energy would require a higher power UV laser [58].

One other major limitation of UV-PAM systems is the requirement for acoustic coupling to the sample. This requires samples to be either submerged or to be in direct contact with an ultrasound transducer, either one of which could limit the application of this modality in certain use cases.

Chapter 3

Ultraviolet Photoacoustic Remote Sensing Microscopy

This manuscript has been published as N. J. M. Haven, K. L. Bell, P. Kedarisetti, J. D. Lewis, and R. J. Zemp, "Ultraviolet photoacoustic remote sensing microscopy", Opt. Lett. 44, 3586-3589 (2019). Some of the contents have been modified for this thesis.

Abstract

Traditional histopathology involves fixing, sectioning and staining protocols that are time consuming and subject to staining variability. Here we present ultraviolet photoacoustic remote sensing (UV-PARS) microscopy, which is capable of imaging cell nuclei without the need for exogenous stains or labelling. Our reflection-mode approach is non-contact and has the potential to provide useful histological information without laborious sample preparation steps. Tumor cell cultures and excised tissue samples were imaged with 0.7-µm resolution and signal-to-noise ratios as high as 53-dB with close agreement to traditional H&E staining.

3.1 Introduction

Brightfield microscopy in conjunction with tissue fixation, sectioning, and staining, has been the primary means of histopathological examination and cell imaging for over a century. However, these sample preparation steps are laborious, time-consuming and costly, with significant economic burden. Furthermore, such histological processing also delays diagnosis on procedures such as oncological surgery, where histopathology is used as a gold standard to inform surgeons as to the completeness of tumor resection. Due to its time-consuming nature, histology cannot be used as an intraoperative tool to analyze entire resection samples. As such, there is an unmet need for an intraoperative imaging technique that can be performed non-contact and label-free. For example, in as many as 20-40% of breast-conserving surgeries, residual tumor tissues are identified in post-operative pathology, necessitating additional surgeries [55]. Besides being a major economic burden to the healthcare system, these additional surgeries result in added emotional and physical distress to patients that could in some cases ultimately be avoided. Moreover, discordance between pathologists has been partially attributed to staining variability and the skill of the histology personnel [59]. These unmet needs motivate the need for new approaches for label-free histopathological imaging.

Recently, by taking advantage of the intrinsic optical absorption contrast of DNA at ultraviolet (UV) wavelengths, the ability to image cell nuclei in tissue samples has been demonstrated without the use of exogenous staining using UV photoacoustic microscopy (PAM) [54, 56, 57, 60]. In PAM, an excitation beam is focused onto a sample and the resulting absorption generates acoustic waves that can be detected via an ultrasound transducer [10]. Recent UV-PAM approaches have used multiple excitation spots and parallel readout, as well as fast optical scanning to improve readout speeds [55, 58]. While PAM does not require tissue processing or staining, as required in conventional histology, dependence on the

detection of propagating acoustic signals, resulting in the need for direct acoustic coupling to the sample may limit intraoperative usage.

Other approaches aimed at imaging tissue pathology includes multi-photon microscopy, nonlinear microscopy and stimulated Raman microscopy [61, 62], Microscopy with Ultraviolet Surface Excitation (MUSE) [23], light-sheet microscopy [30], optical coherence tomography (OCT) [1, 63], Coherent Anti-Stokes Raman (CARS) microscopy [64], and confocal reflectance microscopy [65], among others. OCT and confocal reflectance microscopy provide scattering rather than absorption contrast and have not yet provided sufficient specificity or agreement with traditional H&E (Hematoxylin and Eosin) pathology. Most nonlinear microscopy methods as well as MUSE and light-sheet microscopy require special staining protocols, which may be outside typical workflows in pathology labs.

We recently introduced a novel label-free imaging modality called photoacoustic remote sensing (PARS) microscopy. PARS is a fundamentally new imaging technology that optically forms images of absorbing structures in scattering tissues, as demonstrated by Hajireza et al. It detects initial pressures generated by a pulsed excitation beam using a detection beam co-focused and co-scanned with the excitation beam [19]. As a result, the PARS approach offers all-optical imaging without the need for direct acoustic coupling. PARS microscopy has been used in several applications, including in vivo structural and functional imaging of microvasculature and tumor imaging [19, 21]. PARS modeling has been in explained in [66, 67]. PARS signal contrast was previously found to be proportional to not only optical absorption but also refractive index mismatches [19]. It is known that cell nuclei and cytoplasm have a refractive index contrast, which may contribute to the observed PARS signals [68]. Here we report a new PARS microscopy system architecture that uses a UV excitation beam rather than the visible light excitation used in previous PARS systems. Yao et al. explored the optimal wavelengths to be used for UV-PAM and found that the 245-275-nm wavelength range was most appropriate [53]. We choose 266-nm because it is

close to a DNA absorption peak and is commonly available with significant power and high-repetition rate due to being a harmonic of Nd:YAG laser fundamental output and related laser technologies. Our approach uses custom frequency doubling of a high-repetition rate green fiber laser.

3.2 Experimental Set-up

3.2.1 Optical System Set-up

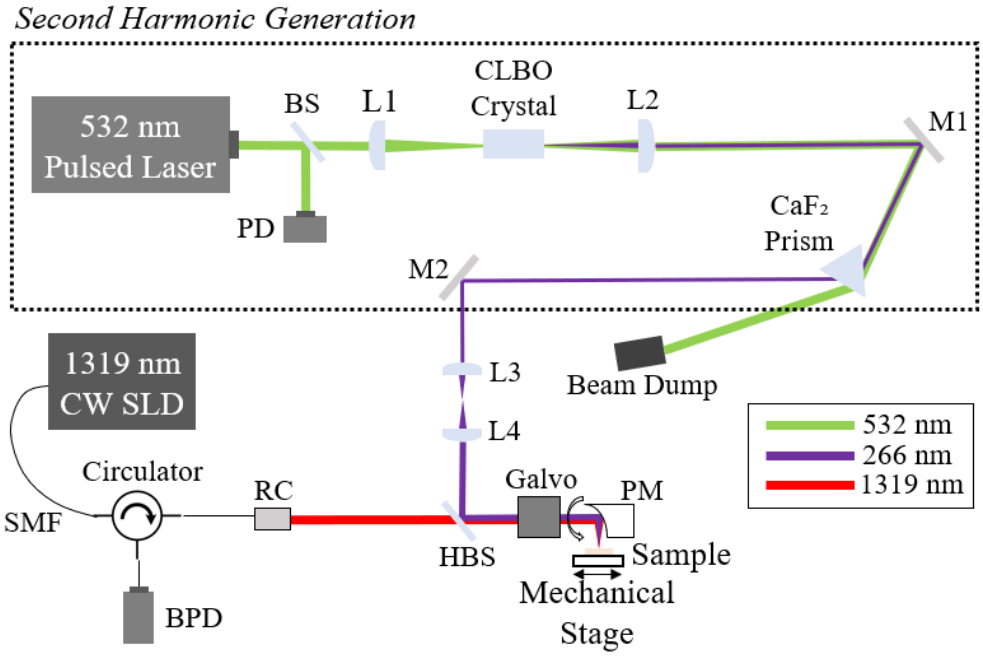

Figure 3.1: UV-PARS experimental set-up. The second harmonic generation boxed section encompasses components used primarily for generation of the 266-nm ultraviolet excitation source. BS – beam splitter; L – lens; M – mirror; SMF – single mode fiber; PD – photodiode; BPD – balanced photodiode; RC – reflective collimator; HBS – harmonic beam splitter; PM – parabolic mirror.

Figure 3.1 shows the system setup diagram for UV-PARS. A 20-600-kHz repetition-rate 532-nm pulsed fiber laser delivers nanosecond pulses with up to ~18-μJ pulse energies (at 20-kHz). This excitation beam is split using a low reflection glass slide. The split-off beam is then fed into a 350-MHz photodiode

(DET10A, Thorlabs) for triggering purposes. The remainder of the beam is focused through a 5×5×6-mm Caesium Lithium Borate CLBO non-linear crystal (Eksma Optics) via a plano-convex lens (LA1464-A-ML, Thorlabs). The CLBO crystal was chosen because it enabled a high-repetition rate output and has minimal walk-off angle, resulting in minimized beam ellipticity. Other crystals considered included KTP (Potassium Titanyl Phosphate), which has a transmission range only above ~350-nm, KDP (Potassium Dideuterium Phosphate), which is primarily only used for low-repetition rates (i.e. <100-Hz), and BBO (Barium Borate), which has a larger walk-off angle than CLBO [69]. Our approach did not necessitate the use of a pinhole aperture as commonly used in UV-PAM systems. Using a knife-edge experiment the ellipticity ratio of the output UV beam was determined to be 0.70. This is then recollimated using another plano-convex lens (LA4380-UV-ML, Thorlabs). In order to separate the generated 266-nm light from the remaining 532-nm beam, a UV-transparent CaF_2 equilateral dispersive prism is used (PS862, Thorlabs). At 20kHz repetition rates, with ~2.1-μJ input pulse energy, we obtained ~80-nJ of 266-nm light after passing through this prism. Higher energies and conversion efficiencies were possible but not needed. At 600 kHz, 266-nm pulse energies of ~14-nJ were measured using 5.68-W input power. The generated 266-nm beam then passes through another set of lenses to expand to the desired beam width. A 1319-nm continuous superluminescent diode laser (SLD1018PXL, Thorlabs) with a ~40-μm coherence length is used as an interrogation beam. This beam passes through a circulator (CIR1310PM-APC, Thorlabs) and is then collimated via a reflective collimator (RC04APC-P01, Thorlabs). The 266-nm and 1319-nm beams are then combined via a harmonic beam splitter (HBSY134, Thorlabs), which transmits the 1319-nm beam and reflects the 266-nm beam. Both beams are then routed through a galvanometer scanning system for alignment purposes and then co-focused onto the sample using an off-axis parabolic mirror (MPD00M9-F01, Thorlabs). A parabolic mirror is used rather than a lens to remove chromatic aberration effects which would interfere with the ability to co-focus both beams.

The Galvo system was also used to scan the beams prior to stage scanning to avoid laser damage to the sample which can occur due to repeated exposure of a stationary focused spot. Two linear stages (Micos PLS-85, PI), each driven by a bipolar microstep driver (MBC2508, Anaheim Automation) provided lateral sample movement. The backscattered 1319-nm beam returns after interrogating the sample and is redirected via the circulator to a 75-MHz balanced photodiode (PDB420C-AC, Thorlabs). The balanced functionality of this photodiode is not used, instead the second photodiode is kept at a constant reference. The PARS signal was filtered using a 1.8-MHz high-pass filter (EF509, Thorlabs), as well as an 11-MHz low-pass filter (BLP-10.7+, Mini-circuits). All data is acquired using a data acquisition card (CSE1242, Gage Applied) and the maximum of the envelope-detected PARS signal is recorded for each scan position. In addition to recording PARS signals, which provide primarily optical absorption contrast, we additionally recorded the DC backscattered signal using the monitor output of the balanced photodiode to produce scattering images.

3.2.2 Post-processing Methodology

All post-processing is done in MATLAB. After the data is acquired via the digital acquisition card, a gaussian filter is applied to the raw PARS signal, and the maximum of the Hilbert transform of this data is recorded, where the absolute value of the Hilbert transform provides the envelope-detected PARS signal. In the case of optically scanned images, the galvo slow axis is then fit using a two-term Fourier series, and the fast axis is smoothed using a Savitzky-Golay filter. The peak locations of both the slow axis and fast axis are then determined to select limits of our image, and these slow axis limits, along with our PARS signal, are used to create an interpolant for scattered data points, allowing us to re-create an image. For mechanically scanned images, since our mechanical stage scanning operation is open loop, a predetermined matrix is generated based on the input mechanical stage step sizes and ranges, and corresponding PARS signal values

are assigned to each element following the scanning pattern used. For both cases, further filtering is then applied onto the re-created image, with a median filter, with 2x2 neighborhood size, being used to reduce salt and pepper noise, and an averaging window, with 9x9 neighborhood size, and 2-D gaussian filter for smoothing purposes.

3.2.3 Chromatic Aberration Correction

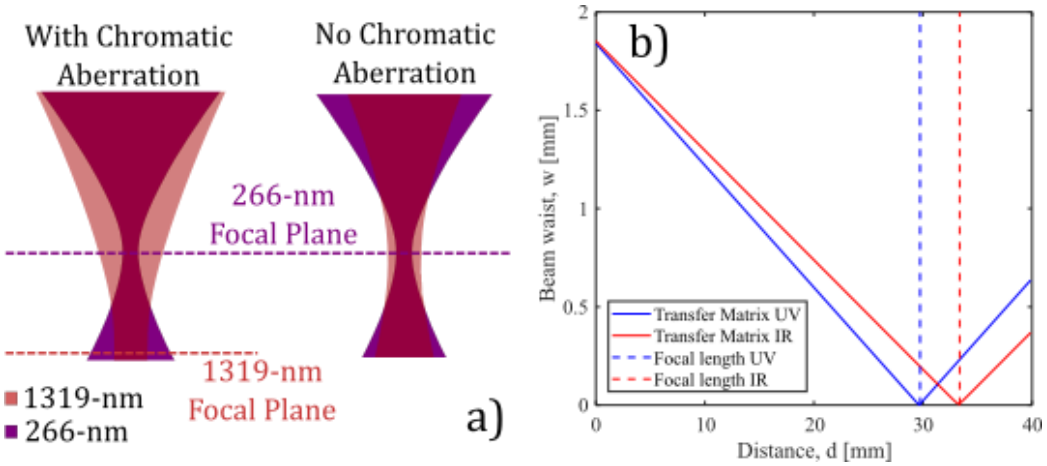

Figure 3.2: Chromatic aberration analysis: a) illustration of representative beam overlap with and without chromatic aberration; b) beam waist versus distance results from our gaussian beam transfer matrix analysis of a standard focusing lens for the interrogation and excitation beams.

Chromatic aberration is the effect that results when a focusing element fails to focus all wavelengths to the same convergence point. This is a result of the wavelength dependence of the index of refraction, which leads to variations in dispersion based on wavelength. Because of the vast difference between the wavelengths we used, almost a 1000-nm difference, the effect of longitudinal chromatic aberration had to be minimized or removed. Figure 3.2a illustrates that with chromatic aberration, the focal planes of each wavelength do not align, and as such, the area of the detection beam at the excitation beam focus is significantly larger than the excitation area, this results in a much weaker

modulated back-scattered detection signal, with substantial detection power loss. In comparison, with no chromatic aberration, when both beams focus to the same plane, there is still a difference in beam area at the focus, however, this difference is considerably smaller. Figure 3.2b shows a plot of beam waist versus distance for our interrogation and excitation beams, calculated using the gaussian beam transfer matrix method for a standard focusing lens (LB4879, Thorlabs). This example results in an illuminated area ratio, that is the area of the interrogation beam over the area of the excitation beam at the excitation focal plane, of 2.17×10^4, illustrating the magnitude of potential lost detection power. In order to address this this problem, we chose to use a parabolic focusing element which does not suffer from chromatic aberration since it is a reflecting element. It is interesting to note that one other advantage it possesses is that it also does not suffer from spherical aberration.

3.3 Phantom Experiments

In order to characterize the resolution of the system, we imaged 100-nm gold nanoparticles as shown in Figure 3.3a. A cross-sectional view of the nanoparticle resolution phantom is shown in Figure 3.3b. Data points were fit using a sum-of-Gaussians, shown as the dotted orange curve. Lateral resolution here is defined as the distance between the peaks of the fitted distribution, where the dip is 0.6 of the maxima ensuring the objects are still distinguishable. A lateral resolution of 0.69-μm was measured which is in close agreement with the theoretical resolution of 0.70-μm based on the Rayleigh criterion, R=0.61λ/NA, calculated for a numerical aperture (NA) of 0.23 (approximated from the input beam diameter and focal length). As the NA of the off-axis parabolic mirror is ~0.4, the resolution can be improved in future work. To further demonstrate the performance of the system, ~7-μm diameter carbon fiber networks were imaged. Figure 3.3c shows one such image where an excitation pulse energy of 10-nJ and

interrogation power 10-mW was used to image the sample. The amplitude signal-to-noise ratio (SNR) was determined to be 67-dB. Where the SNR was determined as follows: $SNR = 20\log_{10}(\mu_{signal}/\sigma_{noise})$, where μ_{signal} is defined as the mean of the signal amplitude in a specific region, and σ_{noise} is defined as the standard deviation of the noise.

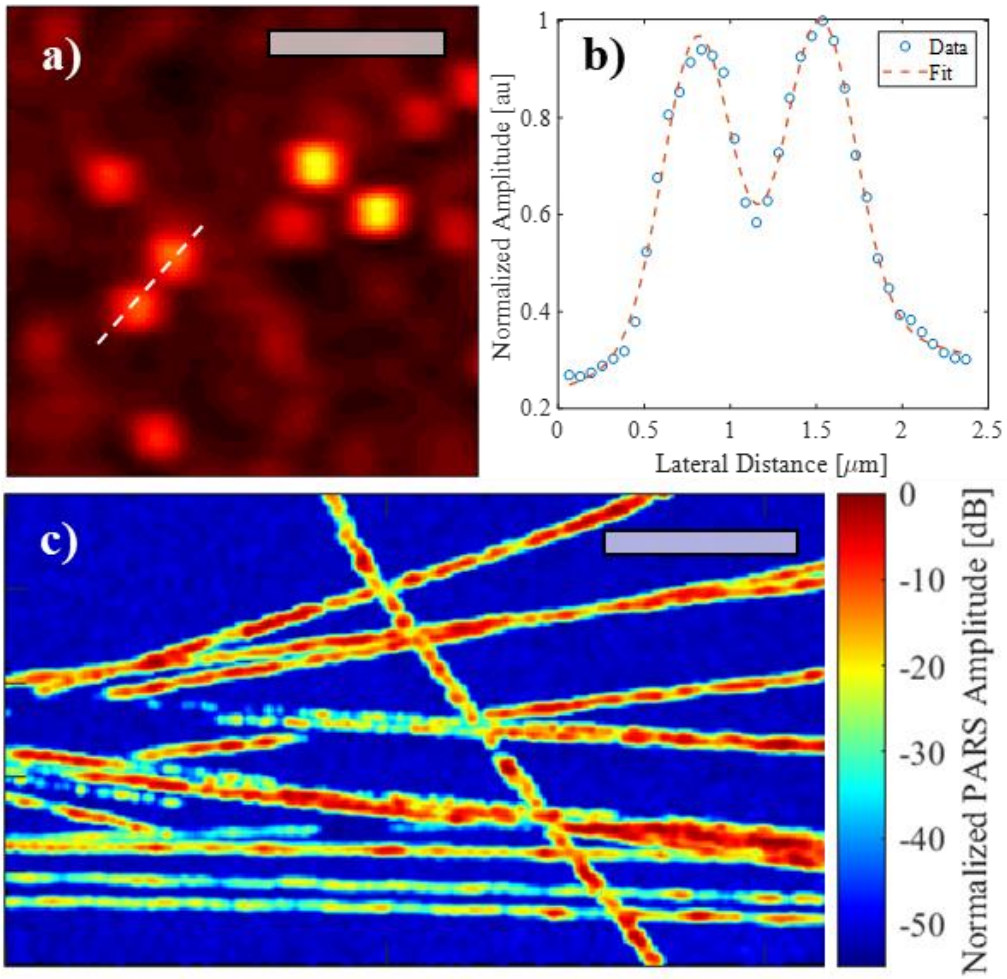

Figure 3.3: Phantom experiment images: a) image of 100-nm gold nanoparticle, scale bar: 2-μm width; b) profile extracted from the white dashed line in a) used to determine lateral resolution; c) image of carbon fiber network, scale bar: 100-μm width.

3.4 Live Cell Culture Experiments

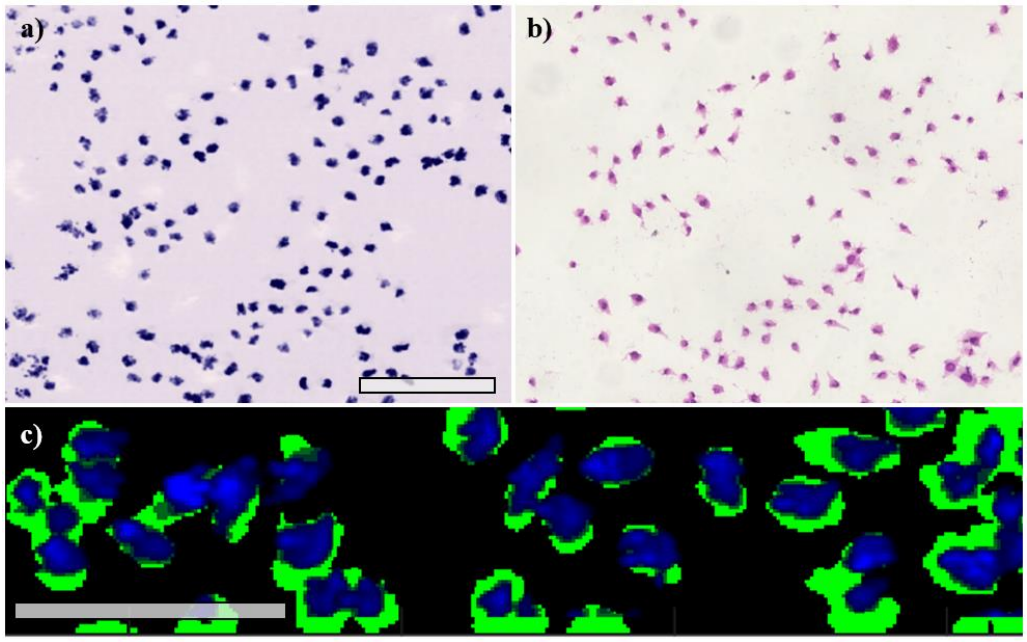

Figure 3.4: HeLa live cell cultures: a) UV-PARS reflection-mode image, scale bar width: 0.2-mm; b) H&E stained sample imaged using transmission-mode brightfield microscopy; c) virtual histology stained image captured with the UV-PARS system, where blue indicates absorption and green indicates scattering, scale bar width: 0.1 mm.

Next, in order to determine the ability of our system to image cell nuclei, HeLa cell cultures (CCL-2, ATCC) of various confluency were imaged. Figure 3.4a shows an image obtained of live HeLa cell cultures using UV-PARS, where an excitation pulse energy of 40-nJ and interrogation power 15-mW was used on the sample. This image can be directly compared to the image in Figure 3.4b which contains the same sample imaged using transmission-mode brightfield microscopy after formalin fixation and H&E staining. Both images are in close agreement with each other. However, it should be noted that since the sample was fixed, stained and imaged following UV-PARS imaging, some cell

detachment occurred. Figure 3.4c shows an image of the superposition of an absorption image, and a scattering image both taken with our system, where the excitation beam was blocked to obtain the scattering image. As can be seen, the scattering image, shown in green, displays the cell body morphology, whereas the UV-PARS image, shown in blue, displays only the cell nuclei, effectively producing a virtually stained image, without the need for exogenous fluorophores or stains. An SNR of 53-dB was obtained for cell culture images taken. These cell culture imaging experiments validate that UV-PARS is indeed imaging cell nuclei.

3.5 Tissue Experiments

To determine the ability of our system to image tissue samples, HT1080 (CCL-121, ATCC) tumors were grown within a chicken embryo chorioallantoic membrane (CAM) model. The tumors were then excised, embedded in optimal cutting temperature compound, and frozen. The frozen samples were then sectioned into 4-μm thick slices, these were then H&E stained after being imaged with our system. Due to the process used to stain the embedded sections, some degradation occurred that can be seen in the comparison images. Figure 3.5a and 3.5c show images of a section taken using UV-PARS. Comparing these directly to the same sample stained and then imaged using transmission-mode brightfield microscopy shown in Figure 3.5b and 3.5d respectively, it can be seen that there is good gross morphology agreement between them. There are also key differences, which may be associated with poor frozen section quality and fixation delay in the H&E image, as well as background UV absorption by cytoplasmic proteins in the UV-PARS image. Figure 3.5e shows a magnified UV-PARS image of a different sample in which individual cell nuclei are observable. These tissue section images indicate great promise for UV-PARS as a new reflection-mode microscopy technology for label-free imaging of tissue pathology.

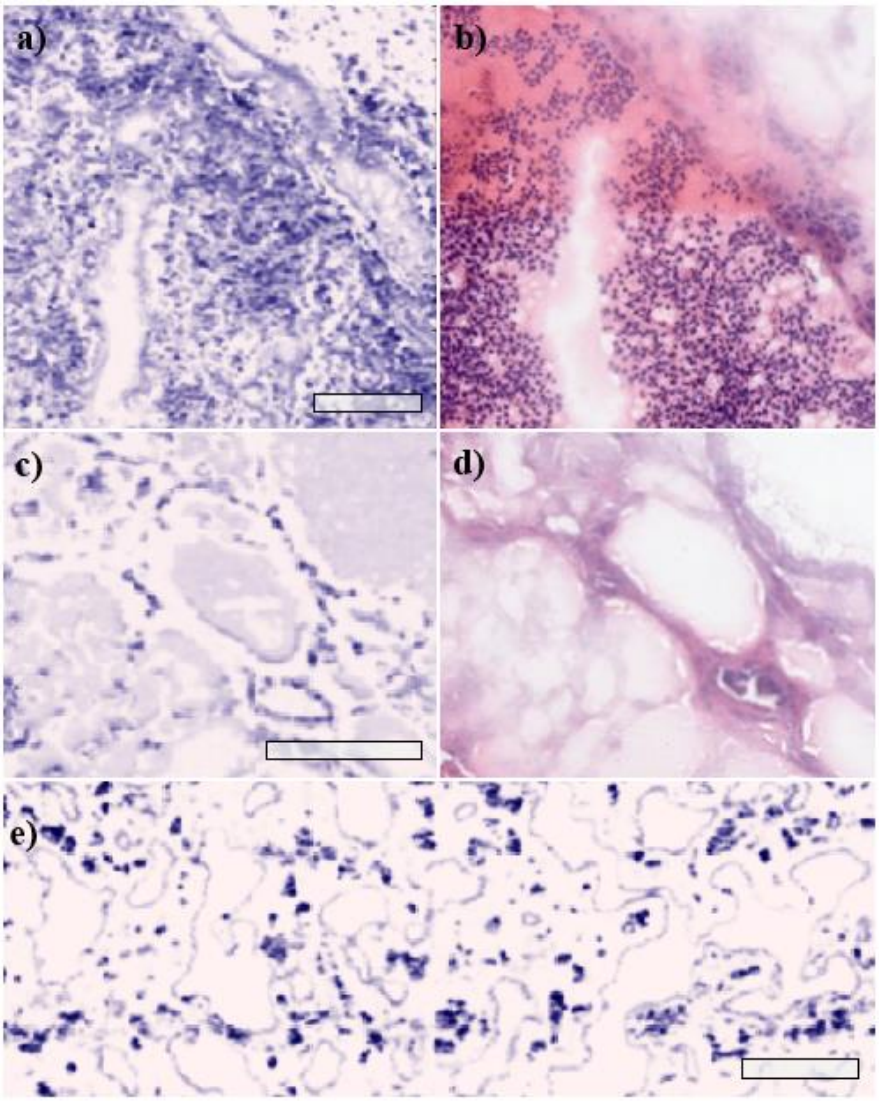

Figure 3.5: Frozen optimal cutting temperature compound embedded HT1080 CAM tumor 4-µm thick tissue section images: a) and c) UV-PARS image, scale bar: 0.1-mm width; b) and d) H&E stained section imaged using transmission-mode brightfield microscopy; e) Magnified UV-PARS image of another tumor section showing individual cell nuclei, scale bar: 0.05-mm width

3.6 Conclusion

Similar to UV-PAM our laser fluences are currently above maximum permissible exposure (MPE) limits for the skin of human subjects [54]. However, main applications of this technology may be for cell imaging and ex vivo tissue imaging where MPE limits do not apply. Subsequent work should aim to further reduce laser exposure to mitigate potential tissue damage for future applications. Future work should also aim to minimize scanning times in order to maximize impact for intraoperative applications. Scanning speed is currently by mechanical stage scanning, this could be greatly improved by using fast optical scanning and higher-repetition rate lasers. Unlike PAM, PARS does not have inherent depth resolution, and as such it relies on the optical depth of focus to provide a measure of optical sectioning. Currently the optical depth of focus (DOF) of our system is ~3-μm, close to the 4-μm thicknesses of standard pathology sections, where the DOF was calculated using $DOF = 2\lambda/\pi(NA)^2$. This is highly promising for future work, which should explore high-NA optical focusing to determine if it is possible to optically section single cell layers from thick tissue samples without the need for sectioning or processing. Previous transmission-mode UV-PAM systems could achieve high-NA optical focusing but required costly UV-transparent fused silica microscope slides and could only be used for thin tissue sections [55]. Our imaging results were obtained in reflection mode and required only standard glass microscope slides. Obtaining high-NA is difficult to achieve using reflection mode PAM systems because of the need to incorporate an ultrasound transducer co-focused with the optical illumination. UV-PARS should be able to achieve very high numerical aperture illumination without the need for any ultrasound transducer or acoustic coupling. The non-contact nature of UV-PARS will surely have practical advantages in workflow, ease-of-use, microscopy system user preference, and potential to combine with other microscope modalities owing to its all-optical nature.

Chapter 4

Reflective Objective-based Ultraviolet Photoacoustic Remote Sensing Virtual Histopathology

This manuscript has been submitted to Optics Letters and is in the review process. Some of the contents have been modified for this thesis.

Abstract

Histopathological examination typically involves tissue resection or biopsy, fixation, sectioning and staining protocols. A non-contact high-resolution photoacoustic remote sensing microscopy system is presented which is capable of imaging cell nuclei in fixed and fresh tissues without the need for stains or labels. The reflection-mode system is based on a 0.5 numerical aperture reflective objective and enables optical scanning to produce histological-like images with 0.39-μm resolution and with close agreement to traditional H&E staining.

4.1 Introduction

Histological examination of tissues and cells by pathologists has remained a gold-standard for disease diagnosis for over a century. Histological examination involves preserving resected or biopsied tissues in a fixative, gross evaluation, cutting, paraffin embedding, sectioning, staining, and slide reading by a pathologist. This laborious and time-consuming procedure results in considerable delays in surgical procedures where malignant tissue must be removed with clean margins. Positive margins are often determined weeks after a surgery, and in as many as 20-40% of solid tumor resections, a repeat surgery is often needed [55]. Such repeat surgeries cost the health-care system billions of dollars each year, cause avoidable patient distress, and could result in a worse severity prognosis. Cryosection pathology is sometimes used intraoperatively to provide feedback on margin status, however, such frozen sections are known to be inaccurate, and cryosectioning is not always feasible with certain fatty tissues which do not section well. Moreover, frozen sections are less preferable as freezing artifacts can impact downstream histological processing [61]. With either cryosectioned or formalin-fixed paraffin-embedded histopathology, there is often significant discordance between pathologists, and histopathological accuracy can depend on several factors such as the skill of the technicians preparing the slides, and staining variability [24]. Thus, there is an urgent unmet need for improved histological imaging technologies, which can rapidly image tissue microstructure, ideally in fresh un-sectioned thick tissues, label-free, and with image quality comparable to traditional histopathology. Such a technology could eventually help inform surgeons of margin status while the patient is still on the operating table, enabling complete removal of cancerous tissue without the need for follow-up surgeries.

Many approaches have been designed to provide alternatives to histopathology with the goal of providing intraoperative virtual pathological diagnosis. These include confocal reflectance microscopy, which however,

provides scattering contrast and thus cannot yet provide specific nuclear contrast [26]. Optical coherence tomography offers millimeter scale imaging depths, but again is based on scattering contrast [1]. Non-linear microscopy including multi-photon autofluorescence, higher harmonic generation, coherent anti-Stokes Raman scattering, and stimulated Raman scattering microscopies can provide histology-like imaging label-free with tight optical sectioning. However, these approaches require expensive ultrafast lasers [3, 70]. Microscopy with ultraviolet (UV) stimulated emission uses fluorescently labelled tissues and UV wide-field illumination. However, optical sectioning capability relies on UV penetration depth, which is tissue dependent, and has trouble differentiating single cell layers [23]. Light sheet fluorescence microscopy has been able to examine fresh thick tissues but suffers from staining variability and in some cases the need for optical clearing agents [30]. Structured illumination fluorescence microscopy has been able to image superficial layers of tissue samples, however, suffers in deeper imaging and also requires exogenous labels [50].

UV Photoacoustic Microscopy (UV-PAM) was recently introduced as a label-free method of imaging cell nuclei in reflection mode, showing an impressive ability to image with histological contrast [54], albeit with the caveat of requiring acoustic coupling with the sample. Moreover, because acoustic detection was required, necessitating partially distinct optical and acoustic paths, light delivery in reflection-mode imaging of thick tissues was typically limited in numerical aperture (NA), thus restricting optical resolution, with a minimum lateral resolution reported as 0.7-μm [54], compared to 0.33-μm in transmission-mode which is not suitable for thick tissue imaging [55]. Axial resolution limitations also resulted in difficulty achieving single-cell layer imaging, however, recent work has moved towards addressing this issue [56, 57]. Additionally, imaging speed was a constraint, nevertheless, new work is aiming to accelerate imaging such as using novel multi-focal-spot light delivery [58]. We recently reported a new non-contact approach, photoacoustic remote sensing, that senses excited photoacoustic initial pressures optically, by detecting refractive index

modulations of a probe beam. This approach was first used to image microvasculature networks with single-cell resolution and has been demonstrated with optical resolution to depths of >2-mm in tissues, as well as for functional imaging [19-21].

For imaging cell nuclei, we recently demonstrated UV-PARS using 266-nm excitation light, where DNA has a strong absorption peak. This permitted imaging of cells and tissues with strong contrast from cell nuclei. This previous UV-PARS system used an off-axis parabolic mirror to focus UV and interrogation light without chromatic aberrations to achieve 0.7-μm spatial resolution [71]. However, the NA of this approach was limited, and the system was not able to use fast optical scanning. Moreover, thick tissue imaging had not yet been demonstrated. In our previous work, and in the previous literature, a main limitation to clinical adoption has been pathologist trust. Images had not yet exhibited sufficiently close correspondence with traditional H&E histopathology. In this letter, we introduce a new optical-scanning reflection-mode UV-PARS system with greatly improved spatial resolution capable of imaging both thin and thick tissues at superficial depths to achieve histopathology-like images without the need for staining. This system uses a 0.5 NA reflective objective lens and galvanometer scanning mirrors to achieve an ultrafine 0.39-μm resolution without chromatic aberration that would otherwise degrade the co-focusing of excitation and interrogation light. This high resolution enables clear visualization of cell nuclear structures that are shown to be in agreement with images of cells and tissues using fluorescent and H&E stains and achieves micron-scale optical sectioning.

4.2 Experimental Set-up

4.2.1 System Set-up

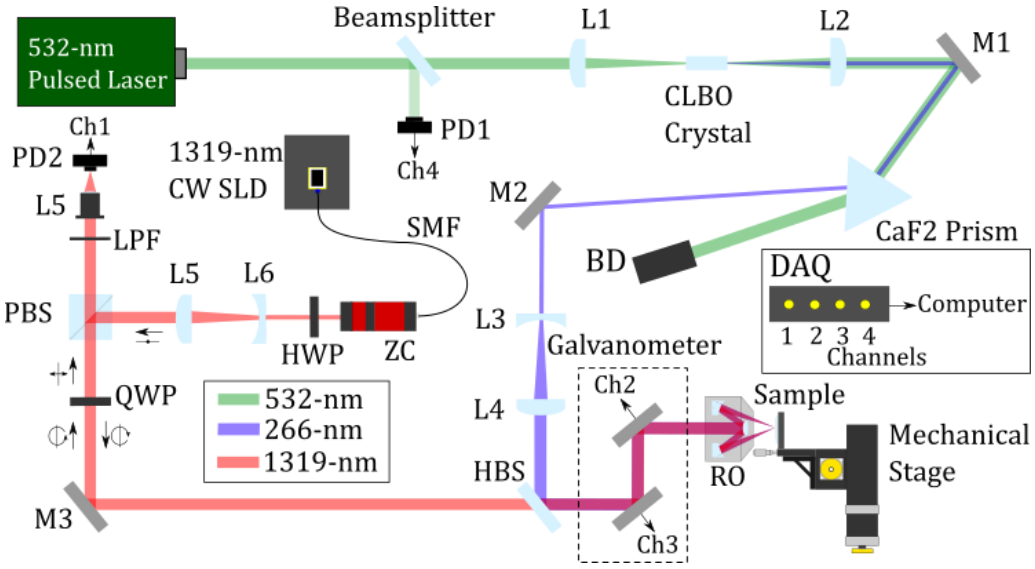

Figure 4.1: UV-PARS experimental set-up. PD – photodiode; L – lens; M – mirror; BD – beam dump; HBS – harmonic beam splitter; RO – reflective objective; QWP – quarter wave plate; PBS – polarization beam splitter; HWP – half wave plate; ZC – zoom collimator; SMF – single-mode fiber; SLD – superluminescent diode; LPF – long-pass filter; DAQ – digital acquisition card.

Figure 4.1 shows the system setup diagram for UV-PARS. A 20-600-kHz repetition-rate 532-nm pulsed fiber laser (GLP-10 , IPG Photonics) delivers nanosecond pulses with up to ~18-μJ pulse energies at 20-kHz. This excitation beam is split using a low reflection glass slide. The split-off beam is then directed towards a 350-MHz photodiode (DET10A, Thorlabs) for triggering purposes. The remainder of the beam is focused through a 5×5×6-mm Caesium Lithium Borate CLBO non-linear crystal (Eksma Optics) via a plano-convex lens (LA1464-A-ML, Thorlabs). The resulting beam is then recollimated using another plano-convex lens (LA4380-UV-ML, Thorlabs). In order to separate the generated 266-nm

light from the remaining 532-nm beam, a UV-transparent CaF2 equilateral dispersive prism is used (PS862, Thorlabs). The generated 266-nm beam then passes through another set of lenses to expand to the desired beam width. A 1319-nm linearly polarized continuous superluminescent diode laser (SLD1018PXL, Thorlabs) with a ~40-μm coherence length is used as the interrogation beam. The single-mode fiber coupled output of this laser diode is collimated using a zoom collimator (ZC618APC-C, Thorlabs), which allows the beam size to be adjusted whilst remaining collimated. A half-wave plate (WPH05-1310, Thorlabs) is then used to adjust the output polarization before it passes through another set of lenses to expand to the desired beam width of 5.1-mm. This beam is then redirected via a polarizing beam splitter (CCM1-PBS254, Thorlabs), where it then passes through a quarter-wave plate (WPQ10M-1310, Thorlabs) converting from linear to circular polarization. The 266-nm and 1319-nm beams are then combined via a harmonic beam splitter (HBSY134, Thorlabs), which transmits the 1319-nm beam and reflects the 266-nm beam. Both beams are then routed through a galvanometer scanning system and then co-focused onto the sample using a UV-enhanced aluminum coated 0.50 NA reflective objective (LMM-40X-UVV, Thorlabs). Here a reflective focusing element is used rather than a refractive focusing element to eliminate chromatic aberration effects which would interfere with the ability to co-focus both beams. Two linear stages (Micos PLS-85, PI), each driven by a bipolar microstep driver (MBC2508, Anaheim Automation) provided lateral sample movement, however, galvanometer optical scanning was the main form of scanning used. The backscattered 1319-nm beam returns after interrogating the sample and due to its reflection, changes polarization handedness, such that when it passes back through the quarter-wave plate, it exits with the opposite linear polarization to its original state. This results in the redirection of the light path via the polarizing beam splitter through a 1250-nm long-pass filter (FELH1250, Thorlabs), which is then focused onto to a 75-MHz balanced photodiode (PDB420C-AC, Thorlabs) using a semi-plan objective (3.2/0.10 160/-, Zeiss). The balanced functionality of this photodiode is not used,

instead the second photodiode is kept at a constant reference. The PARS signal was filtered using a 1.8-MHz high-pass filter (EF509, Thorlabs), as well as an 11-MHz low-pass filter (BLP-10.7+, Mini-circuits). All data is acquired using a data acquisition card (CSE1242, Gage Applied) and the maximum of the envelope-detected PARS signal is recorded for each scan position. In addition to recording PARS signals, which provide primarily optical absorption contrast, we additionally recorded the DC backscattered signal using the monitor output of the balanced photodiode to produce scattering images.

This system differs from our previous report on UV-PARS notably by the use of a reflective objective, and galvanometer-based optical scanning, rather than mechanical scanning, as well as an improved UV beam shape, important for achieving the reported 0.39-μm resolution. These improvements enable the reported fine resolution and optical scanning capabilities important for fast and histologically accurate imaging.

4.2.2 Second Harmonic Generation Characterization

Figure 4.2a shows the obtained UV pulse energies, as well as corresponding conversion efficiencies for different incident pump powers at 20-kHz repetition rate. The data was fit using a single term power series. Pulse energies greater than 150-nJ at 266-nm were measured with a 532-nm input energy above 5-μJ at 20-kHz. Note that the UV power measurements were taken right after the prism output. Since we prioritized beam shape over conversion efficiency these values could have been significantly improved, however, the pulse energies obtained were more than sufficient for our imaging purposes. Note that although we fixed our repetition rate to 20-kHz, UV could also be generated at 600-kHz, with 266-nm pulse energies of ~14-nJ measured using 5.68-W input power.

Next, in order to characterize the beam shape, a knife-edge experiment was carried out. By measuring the power as a function of the position of the blade and then taking the differential of the measurements, we can obtain the beam

profile along a certain axis. Figure 4.2b and c show the results obtained for two orthogonal axes. The original data was fit using a complementary error function which provides confidence of a gaussian output. From these measurements, full-width at half-maximum (FWHM) values of 3.72-mm and 3.51-mm were obtained for the x and y axis respectively. This gives an ellipticity ratio of 0.94 between the y and x axis, suggesting a highly circular beam shape. It should also be noted that the beam size indicated matches well with the desired 5.1-mm input to fill the reflective objective input aperture to maximize our NA.

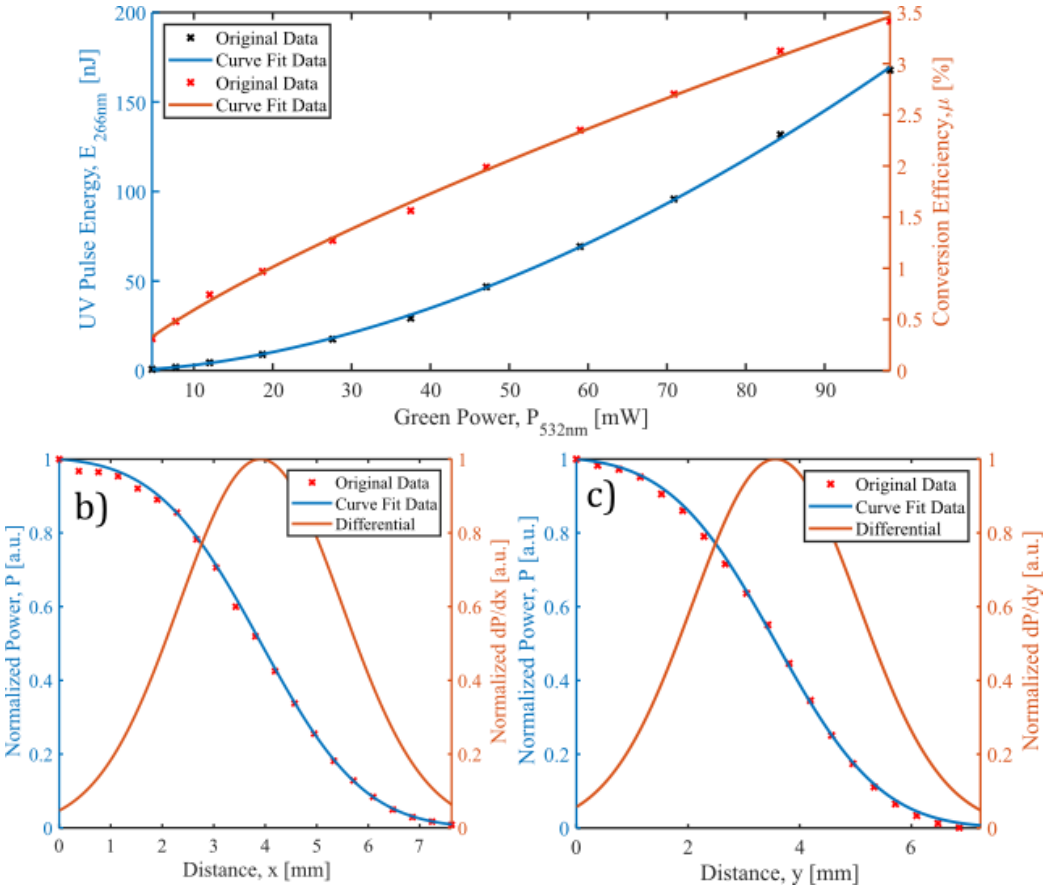

Figure 4.2: UV beam characterization: a) second harmonic generation efficiency and UV pulse energy for a 20-kHz repetition rate input 532-nm beam; b) and c) knife-edge experiment results displaying measured output UV beam shape.

4.3 Results

4.3.1 Phantom Experiment Results

4.3.1.1 Airforce Target Scattering Image

Figure 4.3b shows a scattering image obtained with our system by blocking the excitation path and recording the DC back-scattering signal only. This image was taken using optical scanning and allows us to determine the scale of our images by locating the smallest observable pattern, as shown by the inset in Figure 4.3a. Using this feature, which corresponds to 574.70 cycles per millimetre, we can then determine the distance between the two smallest observable maxima and thus determine the scale of our image.

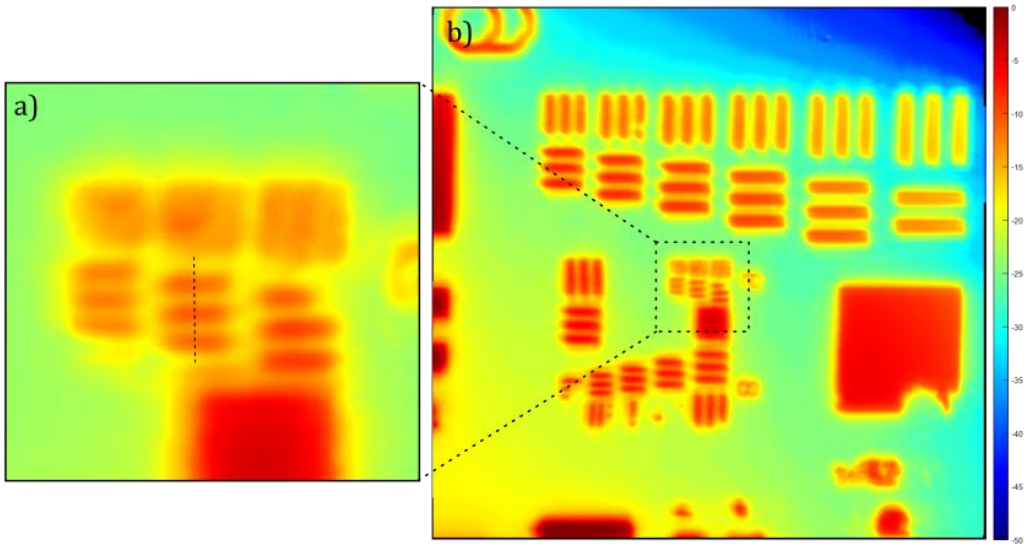

Figure 4.3: Airforce target scattering image a) inset from b) used to determine scale when optical scanning.

4.3.1.2 Resolution Characterization

In order to characterize the resolution of the system, we imaged 100-nm gold nanoparticles as shown in Figure 4.4a. A cross-sectional view of the nanoparticle resolution phantom is shown in Figure 4.4b. Data points were fit using a sum-of-Gaussians, shown as the dotted orange curve. Lateral resolution here is defined as the distance between the peaks of the fitted distribution, where the local minima is 0.7 of the global maxima, ensuring the objects are still distinguishable. A lateral resolution of 0.39-μm was measured which is in close agreement with the theoretical resolution of 0.32-μm based on the Rayleigh criterion, R=0.61λ/NA, calculated for an NA of 0.50.

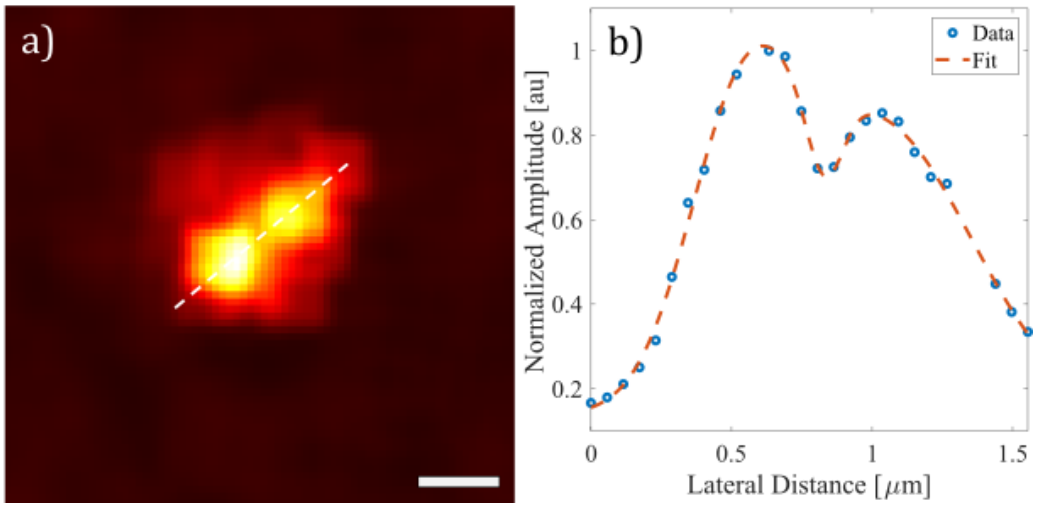

Figure 4.4: Resolution characterization: a) image of 100-nm gold nanoparticle, scale bar: 500-nm width; b) profile extracted from the white dashed line in a) used to determine lateral resolution.

4.3.1.3 Preliminary Optical Sectioning Capability

Since PARS has no inherent depth resolution, we rely on tight optical focusing to give optical sectioning ability. The depth of focus (DOF), calculated using $DOF =$

$2\lambda/\pi(NA)^2$, was found to be on the order of ~0.68-µm for our system. In order to test the optical sectioning capability of our system we imaged ~7-µm diameter carbon fiber networks using mechanical stage scanning where the depth along the network was changed using a micrometer stage. Figure 4.5a shows a maximum amplitude projection image which represents the typical PARS image obtained with no optical sectioning ability. The amplitude signal-to-noise ratio (SNR) was determined to be 55-dB for carbon fiber network images. Where an excitation pulse energy of 3-nJ and interrogation power of 3.24-mW was used to image the sample. Figure 4.5b shows a depth encoded maximum amplitude projection image where it is observable that changes in depth on the order of 6-12-µm display optical sectioning. Since this range falls within the typical diameter of a cell, this indicates that single-cell layer imaging in thick samples could be possible.

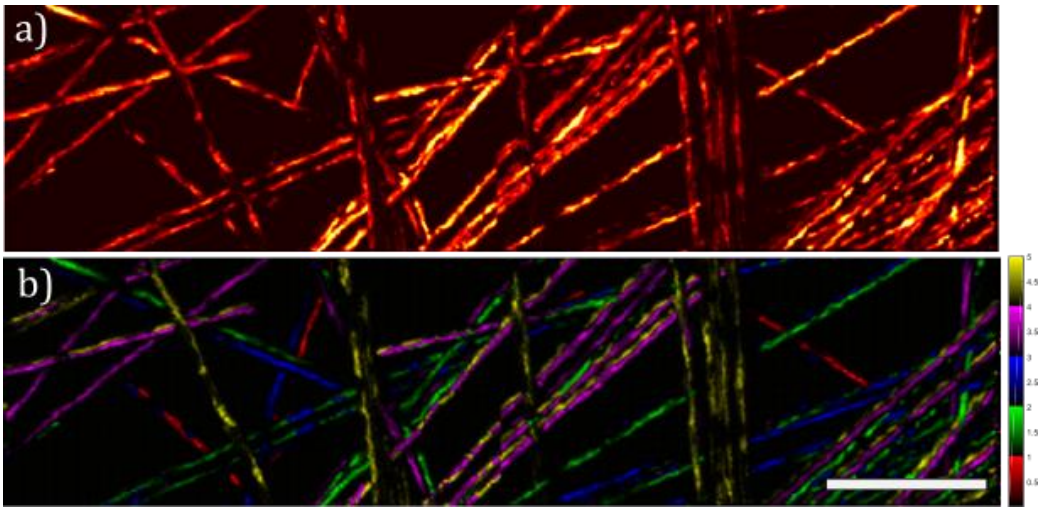

Figure 4.5: Preliminary optical sectioning capability determination: a) maximum amplitude projection image of carbon fiber network; b) depth encoded maximum amplitude projection image, scale bar: 100-µm width. Depth values by color bar: red = 0-µm, green = 12.7-µm, blue = 19.05-µm, pink = 25.4-µm, yellow = 31.75-µm, positive values indicate increasing depth.

4.3.2 Live Cell Culture Experiment Results

4.3.2.1 Live HeLa Cell Culture Imaging

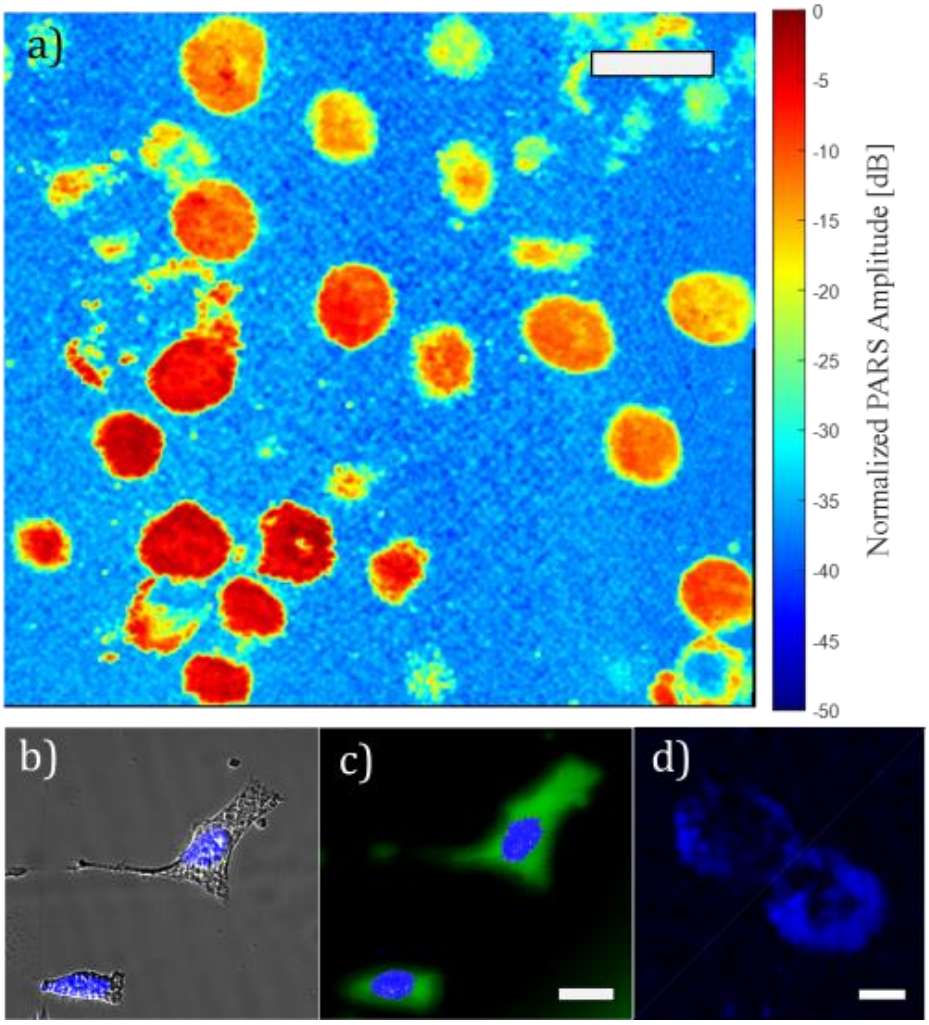

Figure 4.6: HeLa live cell cultures: a) dB-scale UV-PARS reflection-mode image, scale bar: 20-µm width; b) Hoechst fluorescence stained sample imaged using transmission-mode brightfield microscopy; c) virtual fluorescence stained image captured with the UV-PARS system, where blue indicates absorption and green indicates scattering, scale bar: 20-µm width; d) UV-PARS image of fixed dividing HeLa cells, scale bar: 5-µm width.

Next, in order to determine the ability of our system to image cell nuclei, live HeLa cell cultures (CCL-2, ATCC) of various confluency were imaged. Figure 4.6c shows one such image obtained with our UV-PARS system, where an excitation pulse energy of 10-nJ and interrogation power 7.76-mW was used on the sample. Cell culture images were obtained with an SNR on the order of ~42-dB, as seen in Figure 4.6a. The image is a superposition of an absorption image, and a scattering image, where the excitation beam was blocked to obtain the scattering image. The scattering image, shown in green, displays the cell body morphology, whereas the UV-PARS image, shown in blue, displays only the cell nuclei, effectively producing a virtually stained image, without the need for exogenous fluorophores or stains. Comparing our image with that of a brightfield image of the same sample with Hoechst 33342 fluorescence stain overlay as shown in Figure 4.6b shows excellent agreement between the two imaging modalities. Additionally, we were able to capture a UV-PARS image of fixed HeLa cells undergoing mitosis, as seen in Figure 4.6d, which was validated by comparison with Hoechst fluorescence brightfield images. This showcases the potential of this system in the area of cell studies.

4.3.3 Tissue Section Imaging

To determine the ability and versatility of our system to image various tissue types, a number of representative 4-μm thick mouse organ tissue sections were imaged, taken from a hairless SCID mouse (Charles River Nude). These tissues were formalin fixed, followed by embedding in paraffin blocks, and then sectioned. Prior to imaging, paraffin was removed, and the tissue was rehydrated by heating the slides at 60°C for 1 hour, followed by several 2-minute-long washes in 2 changes of xylene, 2 changes of 100% ethanol, 95% ethanol, and finally DI water. A quartz UV-transparent coverslip (CFQ-2220, UQG Optics) was also used

with some DI water to keep the sample hydrated during imaging. All images were obtained using ~5-nJ excitation pulse energy and ~7-mW interrogation power.

Figure 4.7b shows a UV-PARS image obtained of large intestinal villi, when compared to Figure 4.7a showing a neighboring section H&E stained brightfield image of the same sample, it can be seen that there is excellent agreement between the two imaging methods. Note that because we also stained with Eosin, the cytoplasm of the villi is also visible. The UV-PARS image still shows some background signal from the cytoplasm, which is to be expected since RNA and other UV absorbing compounds are still found within these regions albeit, at much lower concentrations. Figure 4.7d shows a UV-PARS image obtained of pulmonary bronchiole. When compared to Figure 4.7c showing a same section hematoxylin stained brightfield image of the same sample, it can be seen that there is again excellent agreement between the two, and that the background signal within cytoplasmic regions is also observable. Figure 4.7f shows a UV-PARS image obtained of pulmonary alveoli, when compared to Figure 4.7e, again showing a same section hematoxylin stained brightfield image of the same sample, it can be seen that there is once more excellent agreement between them. Note that slight discrepancies may be observable between images due to some images being compared to neighboring sections, and for those compared to the same sections, it is expected that the staining procedure could lead to some slight tissue deformity. Furthermore, it is expected that some signal is obtained from hemoglobin from residual blood cells in the tissue.

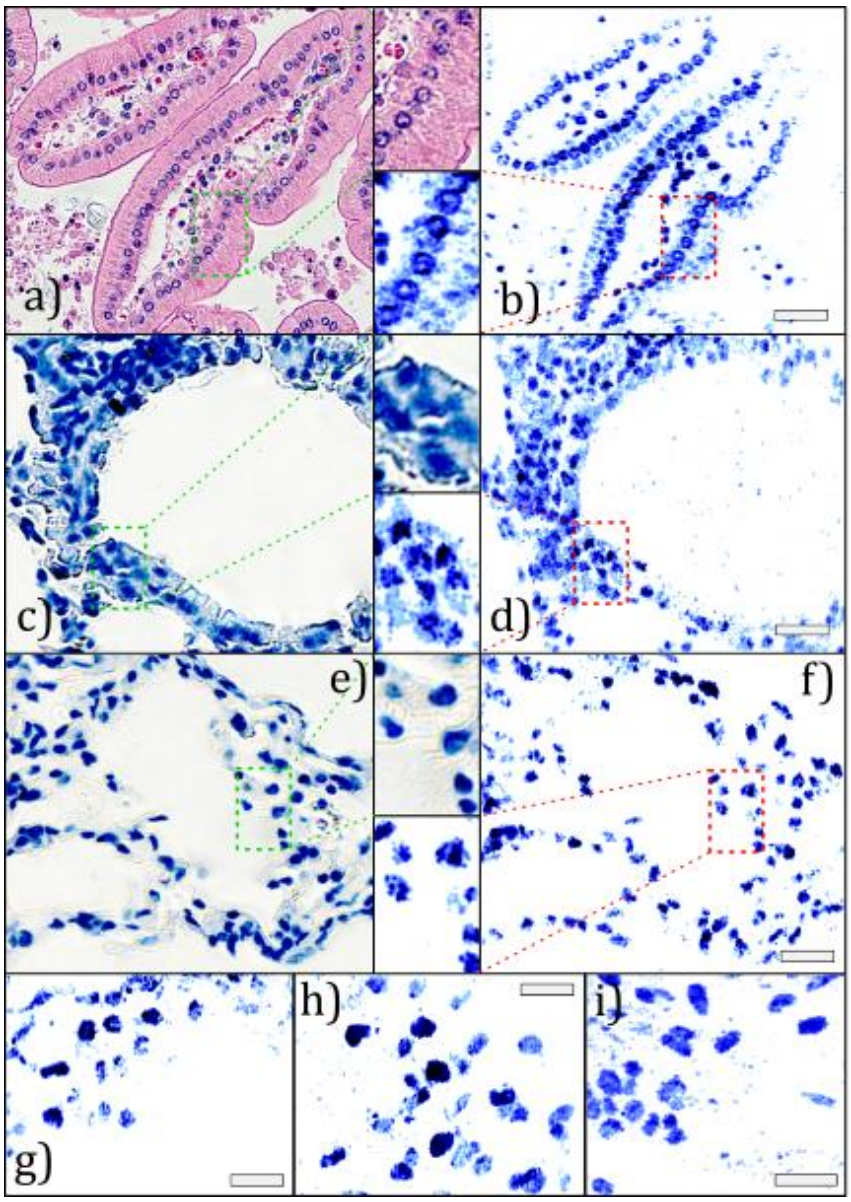

Figure 4.7: 4-µm thick various mouse tissue sections: a) & b) H&E stained brightfield and UV-PARS image of large intestinal villi respectively, scale bar: 30-µm? width; c) & d) hematoxylin stained brightfield and UV-PARS image of pulmonary bronchiole respectively, scale bar: 20-µm width; e) & f) hematoxylin stained brightfield and UV-PARS image of pulmonary alveoli respectively, scale bar: 20-µm width; g) UV-PARS image of 60-µm thick sectioned mouse lung tissue, scale bar: 10-µm width; UV-PARS image of un-sectioned fresh mouse tissue: h) cardiac tissue, scale bar: 10-µm width; i) kidney tissue, scale bar: 10-µm.

In order to demonstrate our ability to image single-cell layers in thick tissue, we imaged 60-µm thick sectioned mouse lung tissue. Figure 4.7g shows our UV-PARS image of this sample, where individual cell nuclei are observable. We next moved on to see the ability of our system to image fresh thick tissue. Figure 4.7h shows a UV-PARS image of fresh un-sectioned cardiac muscle tissue, and Figure 4.7i shows a UV-PARS image of fresh un-sectioned kidney tissue. We can see from both of these images that we can again observe individual cell nuclei. However, although we have seen some success in imaging fresh tissues, obstacles still need to be overcome such as accommodating for surface roughness and curvature. Nevertheless, these initial results showcase the ability to capture a high level of detail, as well as some measure of superficial optical sectioning label-free in a wide variety of tissues.

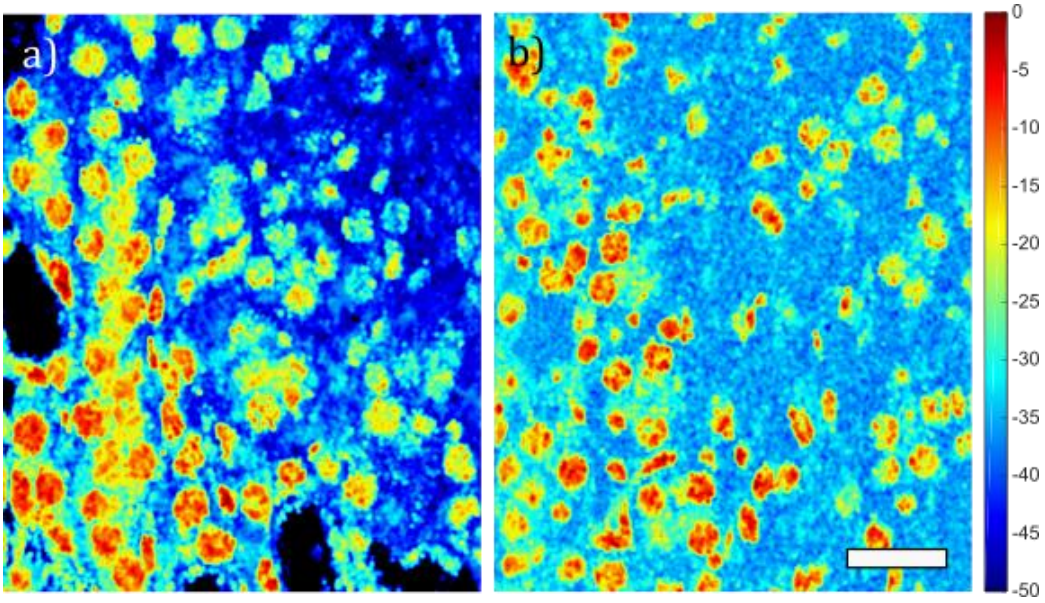

Figure 4.8: dB-scale UV-PARS image of sectioned mouse kidney tissue: a) 4-µm thick; b) 20-µm thick, scale bar: 20-µm width.

Figure 4.8 shows dB-scale UV-PARS images of different thickness sectioned mouse kidney tissue. In both Figure 4.8a and b, individual cell nuclei are observable. It is interesting to note that these images highlight the presence of

some background signal from the surrounding cytoplasm, but nonetheless, are still able to capture cell nuclei with good SNR. Furthermore, the cell nuclei density in Figure 4.8b is comparable to Figure 4.8a, again validating that we are obtaining signal from a single cell layer in the 25-μm thick tissue section.

4.4 Conclusion

Similar to UV-PAM our laser fluences are currently above Maximum Permissible Exposure (MPE) limits for the skin of human subjects [54]. However, main applications of this technology may be for cell imaging and ex vivo tissue imaging where MPE limits do not apply. Subsequent work should aim to further reduce laser exposure to mitigate potential tissue damage for future applications. Current work primarily exploits DNA contrast similar to hematoxylin staining. Future work should explore other UV wavelengths where protein absorption is dominant for equivalent Eosin staining. Current imaging rate is limited by our 20-600-kHz laser repetition-rate, which determines the pixel readout rate. Higher-repetition rates should be investigated in future work in order to minimize scan times for intraoperative applications.

Chapter 5

Fast Optical Scanning-based Wide-field Photoacoustic Remote Sensing Microscopy

Abstract

Bulky components restrict the utility of photoacoustic remote sensing microscopy due to scanning speed and field-of-view limitations. Two systems are presented, the first capable of wide-field optical-scanning imaging, by using optical focusing prior to galvanometer scanning, obtaining 1-cm x 1-cm carbon fiber bundle images with ~50-dB signal-to-noise ratio. The second, showcasing preliminary work in moving towards a miniaturized scan head by using a 2-axis MEMS-mirror scanning element, moving photoacoustic remote sensing microscopy towards fast wide-field imaging.

5.1 Introduction

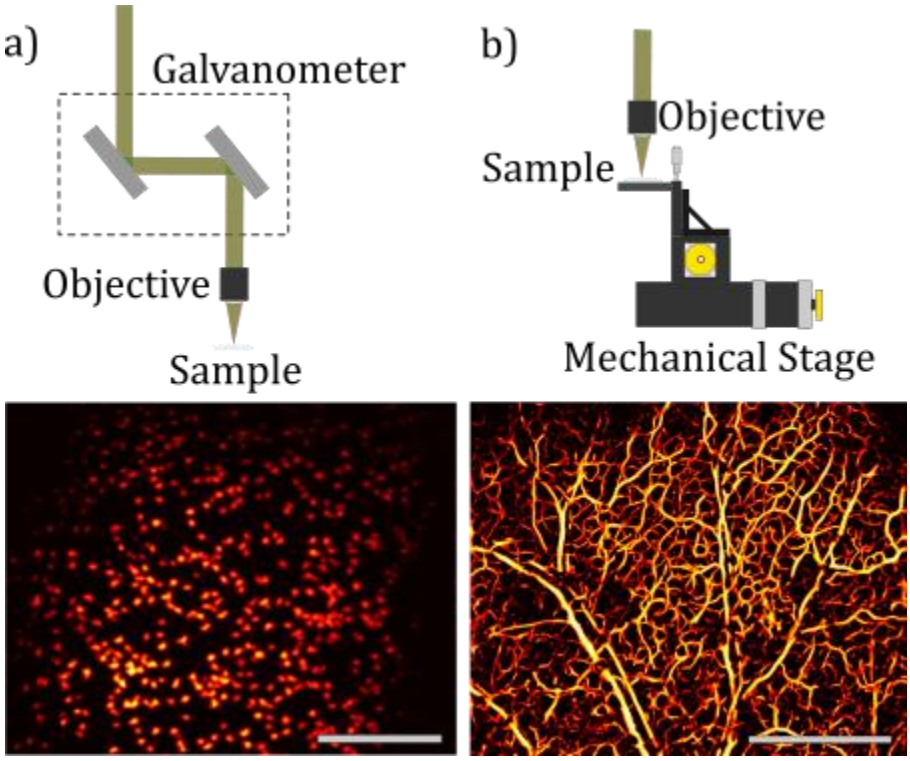

Figure 5.1: Previous PARS scanning methods: a) galvanometer optical scanning, image of mouse red blood cells, scale bar: 100-µm width; b) mechanical stage scanning, image of mouse ear vasculature, scale bar: 600-µm width. Taken with permission from the Zemp lab.

Presently, bulky components restrict the utility of PARS microscopy systems for certain applications including handheld and endoscopic imaging. Additionally, previous embodiments used either mechanical scanning of the sample or optical scanning by steering incident beams into focusing optics. As illustrated in Figure 5.1b, mechanical scanning produces large high-resolution images, however, is slow, being limited by the mechanical stage speed. Optical scanning on the other hand, is typically much faster, especially with the use of resonant scanning mirrors, or polygon scanners. Nevertheless, as shown in Figure 5.1a, optical

scanning can result in degraded resolution far from the central optical axis, limiting the obtainable field-of-view.

Here we present work carried out in several steps. The first step presents a system design that uses optical focusing of beams before the scanning element in order to reduce wide-field aberrations. The second step then implements a system that uses a MEMS scanning mirror to allow for miniaturization of the scanning element. This miniaturization should allow for larger field-of-view imaging due to the shorter optical path taken through the scanning element which would move us towards the ultimate goal of performing fast wide field-of-view imaging that can be translated into our ultraviolet excitation PARS systems presented in the previous 2 chapters.

5.2 Focusing Before Optical Scanning

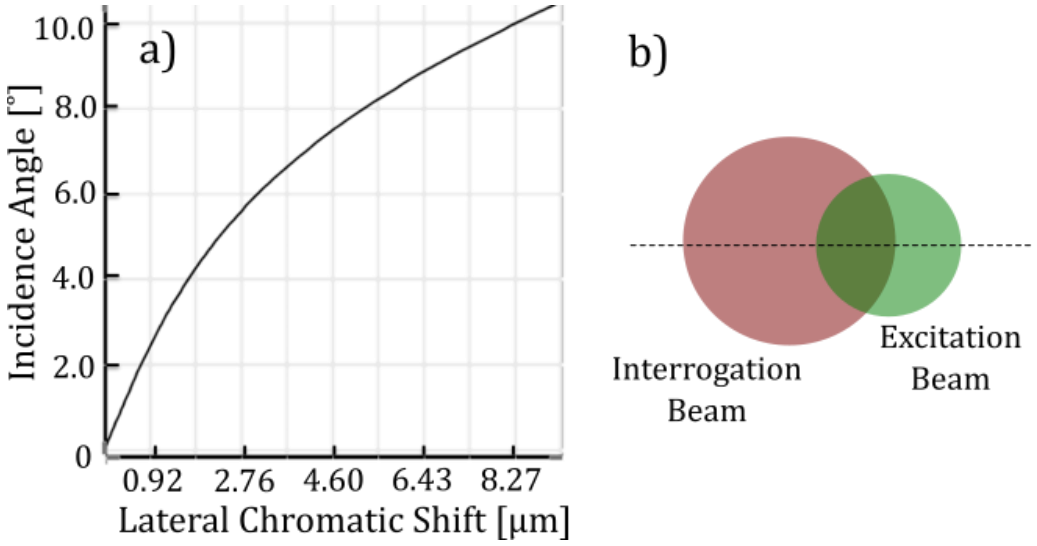

Figure 5.2: Lateral chromatic aberration: a) versus incidence angle for a typical scanning lens (LSM03-VIS, Thorlabs) for 400-nm and 700-nm incident beams; b) visualization of focal spot shift between interrogation and excitation beams.

Our first system design uses optical focusing of beams before galvanometer scanning across the sample. This is superior to other methods of wide-field optical scanning, such as using scanning lenses, because it does not suffer from lateral chromatic aberration which occurs in a system containing such a difference in wavelengths. Figure 5.2a illustrates the magnitude of this effect for a much smaller difference in wavelength, computed using a typical scanning objective (LSM03-VIS, Thorlabs). Figure 5.2b shows the extent that this shift can have on the co-focusing of our interrogation and excitation beams, resulting in significant interrogation power loss. Furthermore, these types of objectives are not typically available for the wavelength range used in our system. One drawback of this method however, is the because the focused beam must travel through the optical scanning element, it requires the use of large working distance objectives, limiting the obtainable lateral resolution, but incidentally increasing the depth of focus, allowing us to obtain larger images less constrained by inherent curvature of the optical scanning path far away from the central optical axis.

5.2.1 Experimental Set-up

Figure 5.3 shows the system setup diagram for the pre-galvo focusing PARS system. A 0.4 to 100-MHz repetition-rate 1030 to 1076-nm tunable pulsed fiber laser (TPL-1060-332-01-UAL01, Genia Photonics) delivers variable width pulses (100-ps to 5-ns). 1064-nm output at 400-kHz and with a 2.5-ns pulse width was used. This excitation beam is collimated using a variable collimator lens and is then focused through a magnesium doped periodically poled lithium niobite (MgO:PPLN) crystal (MSHG1064-0.5, Covesion), which is kept at a constant temperature using a temperature controller (OC2, Covesion). The resulting second harmonic generated 532-nm and remaining 1064-nm are split using a harmonic beam splitter (HBSY21, Thorlabs), where the remaining 1064-nm is fed into a 5-GHz photodiode (DET08CL, Thorlabs) for triggering purposes. A

tunable 1550-nm continuous wave linearly polarized (TLK-L1550R, Thorlabs) laser is used as an interrogation beam. The single-mode fiber coupled output of this laser diode is collimated using a reflective collimator (RC08FC-P01, Thorlabs). A half-wave plate (WPH10M-1550, Thorlabs) is then used to adjust the output polarization before it passes through another set of lenses to expand to the desired beam width. This beam is then redirected via a polarizing beam splitter (CCM1-PBS254, Thorlabs), where it passes through a quarter-wave plate (WPQ10ME-1550, Thorlabs) converting from linear to circular polarization. The 532-nm and 1550-nm beams are then combined via a dichroic mirror (DMSP1000R, Thorlabs), which transmits the 532-nm and reflects the 532-nm beam. Both beams are then co-focused through an uncoated 50-mm focal length plano-convex lens (Thorlabs, LA1131) and optically scanned across the sample using a galvanometer (6230H, Cambridge). The objective lens was chosen for its respectable working distance required since the beam must pass through the galvos before reaching the sample. The backscattered 1550-nm beam returns after interrogating the sample and due to its reflection, changes polarization handedness, so that when it passes back through the quarter-wave plate, it exits with opposite linear polarization to its original state. This results in redirecting of the light via the polarizing beam splitter through a 1550-nm band-pass filter (FBH1550-12, Thorlabs), and then focused onto to a 150-MHz photodiode (PDA10CF, Thorlabs) via a semi-plan objective (3.2/0.10 160/-, Zeiss). The PARS signal was filtered using a 20-kHz high-pass filter (3148, KR Electronics), as well as a 22-MHz low-pass filter (BLP-21.4+, Mini-circuits). The PARS signal is then passed through a pulsar-receiver (5900OR, Olympus), this is used for amplification purposes as well as filtering purposes. All data is acquired using a data acquisition card (CSE1242, Gage Applied) and the maximum of the envelope-detected PARS signal is recorded for each scan position. Note that a free-space design was used for this system due to the narrow band nature of the 1550-nm, which resulted in highly coherent light leading to interference effects when using a circulator.

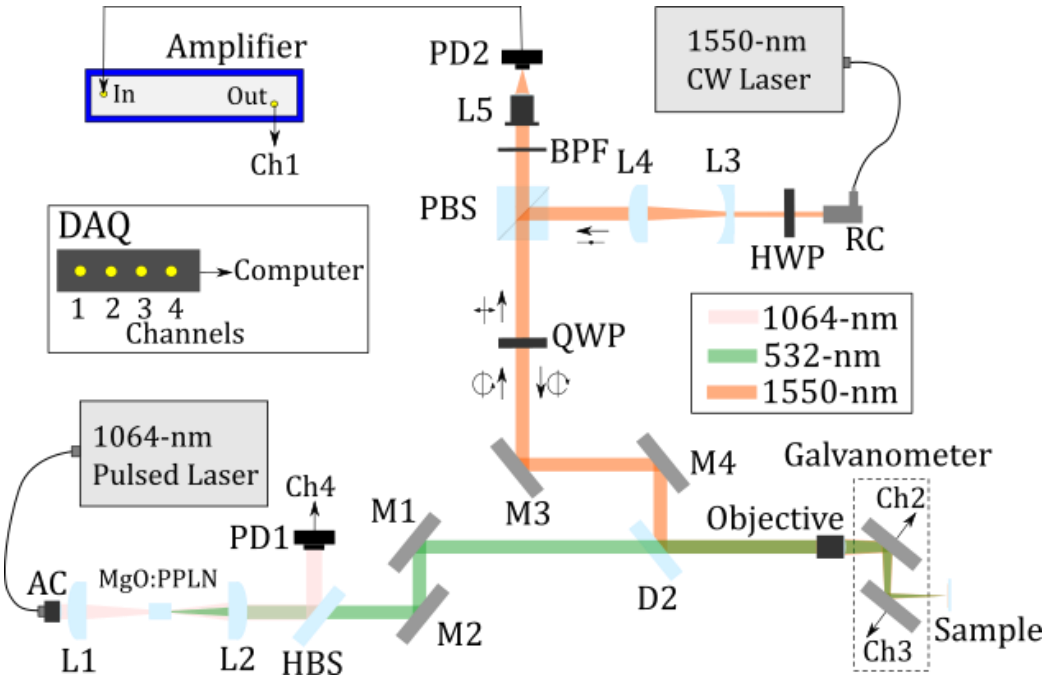

Figure 5.3: Pre-galvo focusing PARS experimental set-up. L – lens; M – mirror; PD – photodiode; D – dichroic; AC – adjustable collimator; PPLN – periodically poled lithium niobite; QWP – quarter-wave plate; PBS – polarization beam-splitter; HWP – half-wave plate; BPF – band-pass filter; DAQ – data acquisition card.

5.2.2 Experimental Results

In order to test the imaging capability of our system, a bundle of 7-µm diameter carbon fibers was imaged. Images were taken using 532-nm excitation with 2.5-ns pulse width at 400-kHz. Figure 5.8 shows a representative image obtained with our system, exhibiting an SNR of ~50-dB for a field-of-view of ~1-cm x 1-cm, showcasing that the method of focusing prior to galvo scanning is a very effective way to achieve large field-of-view images. It should be noted however that since we are imaging carbon fiber bundles, the outer regions of the image will most likely correspond to different layers within the bundles, which we area able to capture due to the large depth of focus that follows the use of a large focal length objective. Following from this, we would expect that the use of a higher

numerical aperture objective, with a tighter depth of focus would have a significantly decreased field-of-view, albeit with higher resolution.

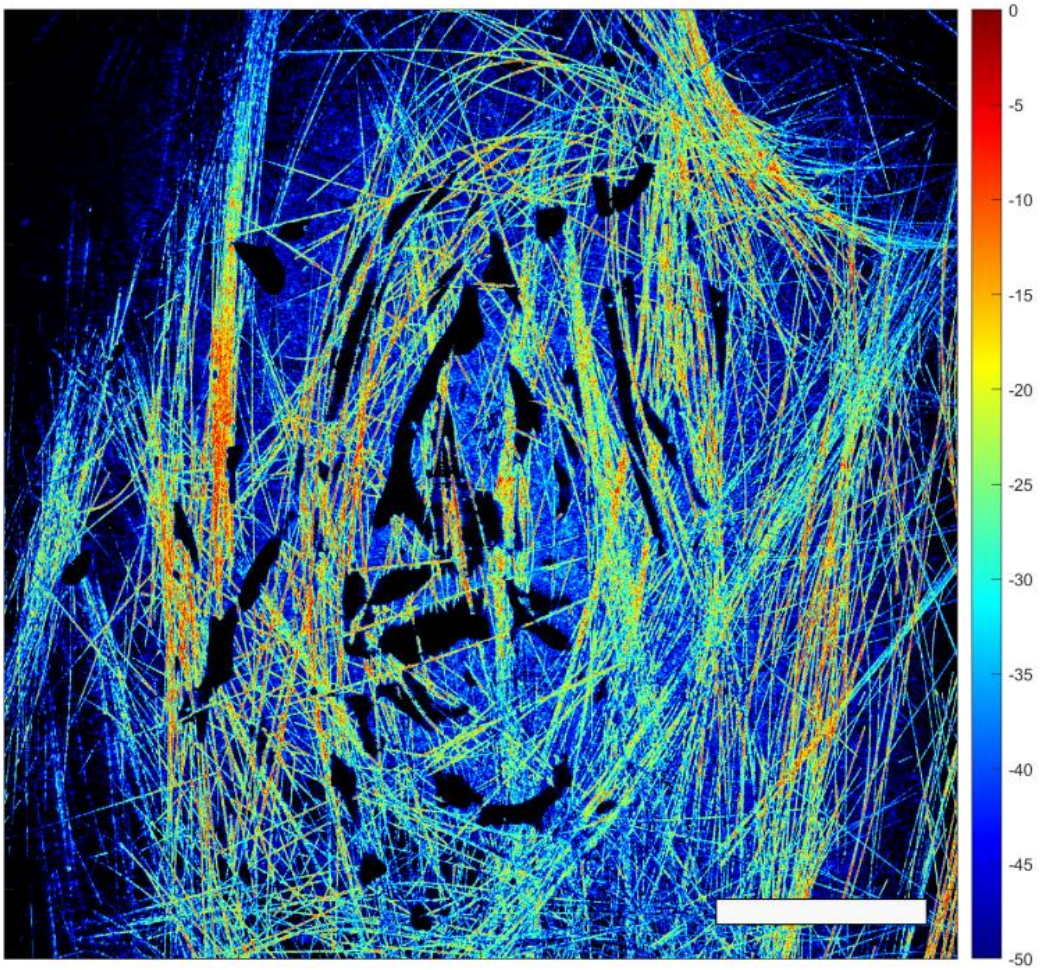

Figure 5.4: PARS image of carbon fiber bundle using pre-galvo optical focusing, scale bar: 2-mm width.

5.3 MEMS-mirror Optical Scanning

For our second system, we moved towards a MEMS scanning mirror design, in order to allow for miniaturization of the scanning element. The purpose for this miniaturization is to allow for larger field-of-view imaging due to the shorter optical path taken through the scanning element. Because of this shorter optical

path requirement, it also should result in an ability to use shorter working distance, or higher numerical aperture objective lenses, allowing us to obtain higher resolution images over a larger field-of-view than would normally be obtainable.

5.3.1 Experimental Set-up

5.3.1.1 System Set-up

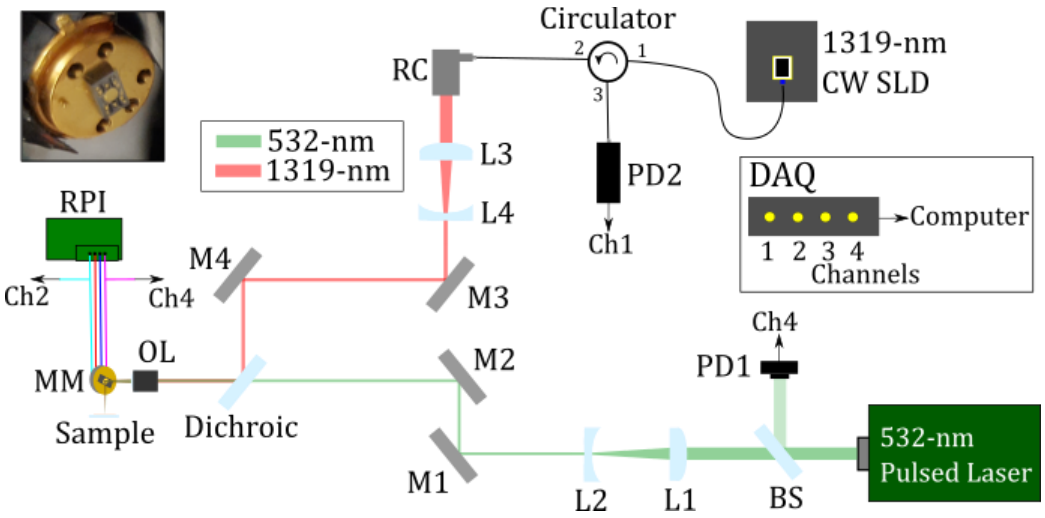

Figure 5.5: MEMS-PARS experimental set-up. BS – beam splitter; L – lens; M – mirror; PD – photodiode; RC – reflective collimator; SLD – superluminescent diode; OL – objective lens; MM – MEMS mirror; RPI – Raspberry Pi; DAQ – data acquisition card. Top left inset displays an image of the MEMS mirror itself with the window removed.

Figure 5.5 shows the setup diagram for the MEMS-PARS system. A 20-600-kHz repetition-rate 532-nm pulsed fiber laser delivers nanosecond pulses with up to ~18.35-μJ pulse energies (at 200-kHz). This excitation beam is split using a low reflection glass slide. The split-off beam is then fed into a 350-MHz photodiode (DET10A, Thorlabs) for triggering purposes. The 532-nm beam then passes through a set of lenses to reduce to the desired beam width. A 1319-nm

continuous superluminescent diode laser (SLD1018PXL, Thorlabs) with a ~40-μm coherence length is used as an interrogation beam. This beam passes through a circulator (CIR1310PM-APC, Thorlabs) and is then collimated via a reflective collimator (RC04APC-P01, Thorlabs). The beam then passes through a set of lenses to reduce to the desired beam width. The 532-nm and 1319-nm beams are then combined via a dichroic mirror (DMSP-1000R, Thorlabs), which transmits the 532-nm beam and reflects the 1319-nm beam. Both beams are then co-focused via an aspheric lens (AL1225, Thorlabs) and reflected off of a 1-mm diameter gold-coated 2-axis MEMS mirror (TF31, Precisely) with the window removed to optically scan across the sample. The MEMS mirror is controlled using a raspberry pi equipped with a custom driver board, with pick-off wires being used to probe the current mirror position. The backscattered 1319-nm beam returns after interrogating the sample and is redirected via the circulator to a 75-MHz balanced photodiode (PDB420C-AC, Thorlabs). The balanced functionality of this photodiode is not used, instead the second photodiode is kept at a constant reference. The PARS signal was filtered using a 1.8 MHz high-pass filter (EF509, Thorlabs), as well as an 11-MHz low-pass filter (BLP-10.7+, Mini-circuits). All data is acquired using a data acquisition card (CSE1242, Gage Applied) and the maximum of the envelope-detected PARS signal is recorded for each scan position. It should be noted that beam reduction was required here due to the small size of the MEMS mirror diameter to reduce beam clipping, which had a negative impact on the resolution of the system.

5.3.1.2 MEMS-mirror Set-up

The 2-axis MEMS mirror deflection is controlled by varying the voltage across four channels. Where 2 channels control the -x and +x axis and the other 2 channels control the -y and +y axis. In order to characterize the deflection angle response of each axis against input voltage, the MEMS mirror was positioned such that its face was at a 45° angle to an incident laser beam, this laser beam was

then reflected across the room onto a board where measurements of position could be made. By measuring the displacement as the voltage applied across the MEMS mirror was changed and knowing the distance the mirror was away from this board, an estimate for the angle deflection could be made. Figure 5.6a shows the characterization results carried out for each axis. From this graph it is obvious that the relationship is non-linear.

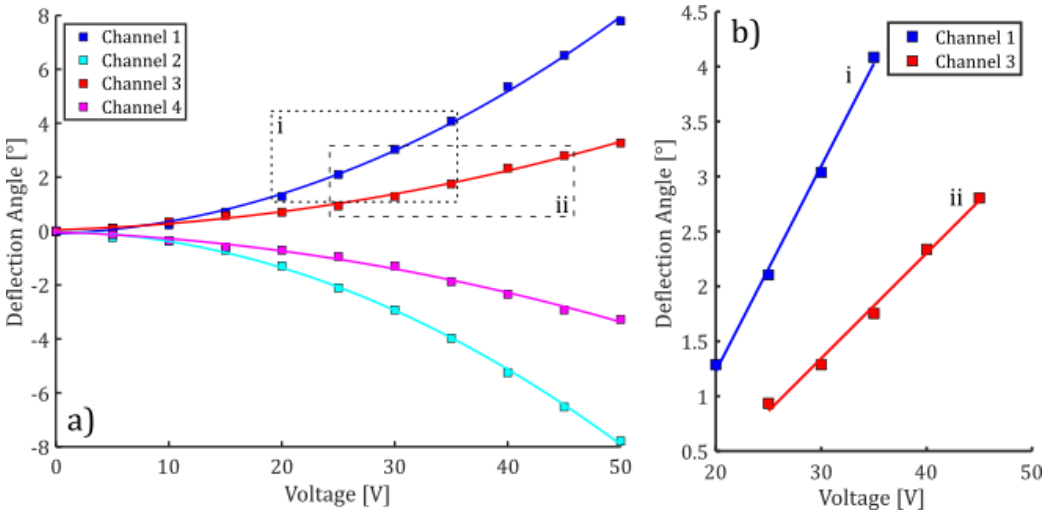

Figure 5.6: MEMS scanning mirror axis characterization: a) over full range for all channels; b) inset corresponding to boxes i and ii in a).

This non-linearity posed a problem in reconstruction of our image. Originally, to combat this, the non-linearity was characterized, and then a correction could be made in post-processing to determine the actual location of our imaging points. However, due to imperfect characterization of the deflection angle as a function of input voltage, the results were not satisfactory. The next approach was to linearize the output, where instead of stepping in equal input voltage increments, we stepped in equal deflection angle increments, which required back-calculating voltages at which these deflection angles occur. However, this approach was again dependent on the characterization we performed, and as such did not give acceptable results. Eventually, a different approach was taken, that solved

another issue, whereby instability in scanning occurred when scanning through the center of the mirror with all channels active, and especially when scanning over larger deflection angles at higher frequencies. This was solved by only using 2 channels, one for each positive axis and operating the mirror at higher voltages within regions of linear response as shown in Figure 5.6b. The disadvantage of this approach was that it resulted in a limited deflection angle, however, the increased stability was a more important factor for reliable imaging.

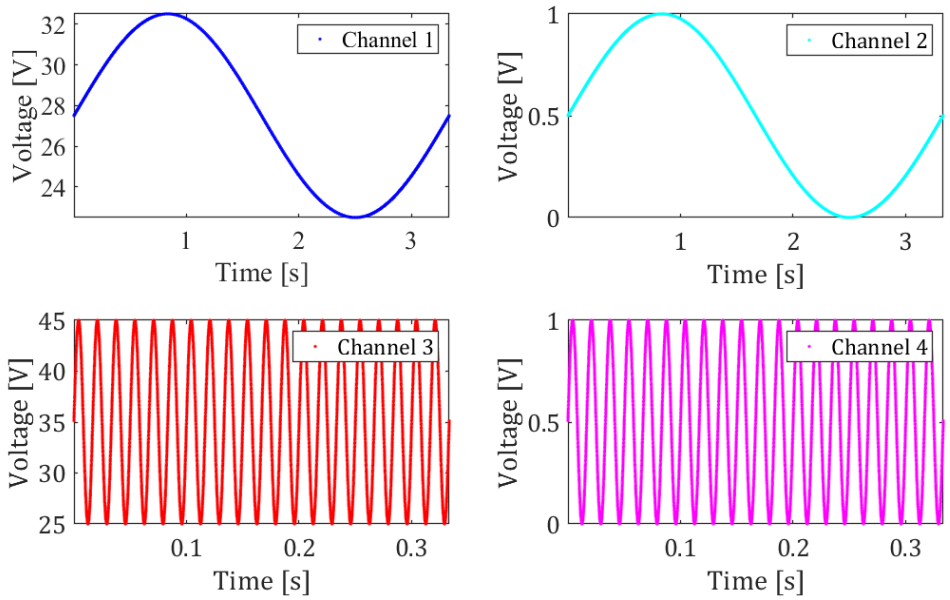

Figure 5.7: Typical waveforms generated in all channels to drive the MEMS scanning mirror. Note channels 3 and 4 have been shortened for clarity.

One advantage of staying within the linear region arises from the fact that the driver board could only output positive voltage values for each channel, thus, since the linear region is off-set from the centre, a sinusoidal wave could be generated around this off-set with only 2 channels required to control the MEMS mirror. Furthermore, due to the high voltages required to drive the MEMS mirror, the other 2 channels could be set to the same waveforms as their counterparts, but at much lower voltages to lower the noise floor of the digital

acquisition card considerably. This is shown in Figure 5.7, where channel 1 and 3 were used to drive the MEMS mirror, and channels 2 and 4 were used as a probe input to the digital acquisition card. This was required since the MEMS mirror operated in open-loop without any deflection-angle feedback. It should also be noted that the voltage range for channels 1 and 3 were selectively determined to ensure a symmetric scan pattern, in other words equal deflection angle range in the x and y axis.

In order to obtain these input voltages, a 3-column .csv file, with the first column representing the channel number, second column representing the time, and third representing the voltage was read into a custom script run on a raspberry pi that drove a custom Precisely driver board to output our desired waveforms to the MEMS mirror. Due to the requirement of a .csv file, memory limitations restricted the slowest frequency that could be run to 0.3-Hz, as a result, for a reasonable image point density, our 532-nm source had to be run at 200-kHz.

5.3.2 Experimental Results

To test the imaging capability of our system, a bundle of 7-μm diameter carbon fibers was imaged. Images were taken using ~100-nJ 532-nm excitation pulse energies at 200-kHz, with ~10-mW 1319-nm detection power. Figure 5.8a shows a representative image obtained with our system, exhibiting an SNR of ~42-dB for a field-of-view of ~0.25-mm x 0.25-mm. This image also appears to show products of instability, where wiggles can be seen along the carbon fibers, suggesting that there could have been some mirror deflection instability. Since the MEMS mirror is operated in open loop, these instabilities are not accounted for.

One way to attempt to remove these instability artifacts is to use a Hessian based Frangi vesselness filter, which was applied in post-processing. Where the Frangi filter uses eigenvectors of the Hessian matrix to determine the probability

of vessels or image ridges being contained within an image region [72]. Figure 5.8b shows the results of this post-processing, where we can see considerable improvement, including a substantial increase in SNR.

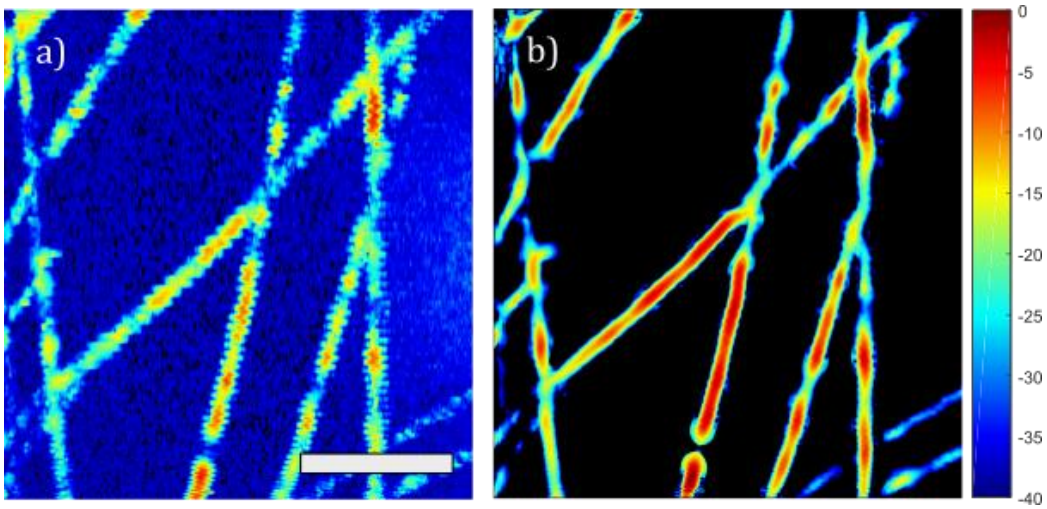

Figure 5.8: PARS image of carbon fibers using MEMS optical scanning: a) without Frangi filter; b) with Frangi filter, scale bar: 70-µm width.

5.4 Conclusion

Overall, we demonstrated the potential to obtain wide field-of-view images using optical focusing prior to scanning, albeit with a trade-off between lateral resolution and field-of-view, partially dependent on the depth of focus as well as on the focal length. Next, we moved towards replacing typical galvanometer optical scanning for a 2-axis MEMS scanning mirror, significantly reducing the path length our beam has to travel through our scanning element. Unfortunately, the small 1-mm diameter MEMS mirror limited the achievable field-of-view. Figure 5.9a and b help to illustrate the reason for this problem, where the field-of-view was limited by the distance between the focus and point where the beam width reaches $\sqrt{2}/2$-mm (for our 1-mm diameter mirror). This limitation constrained us to using a larger than optimal focal length objective, which

degraded resolution, while still resulting in a poor field-of-view due to the mirror still needing to be close to the focus. Figure 5.9c demonstrates how a bigger mirror would solve these issues and would be key in bringing us closer to integrating this optical scanning technique into our UV-PARS system architecture for fast wide field-of-view histology-like imaging of tissue samples. This describes future work that will be required in order to move UV-PARS towards clinical translation, where fast imaging is required for intraoperative potential.

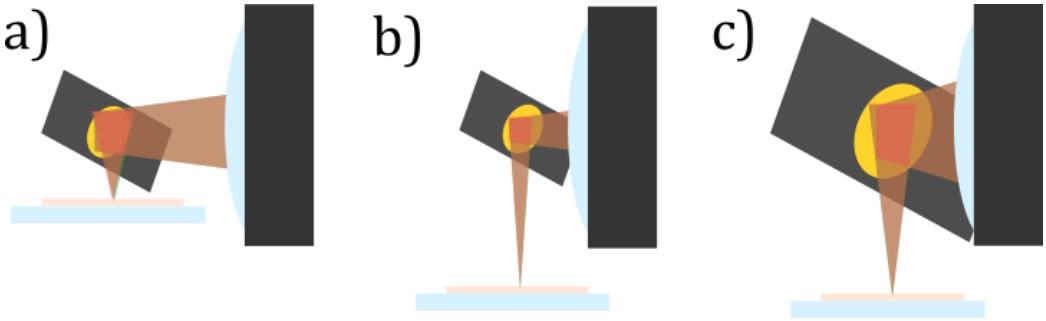

Figure 5.9: Different MEMS scanning mirror set-ups: a) small diameter mirror with tighter focus resulting in greater resolution, but poorer field-of-view; b) small diameter mirror with loose focus resulting in larger field-of-view, but poorer resolution; c) large diameter mirror with tighter focus resulting in larger field-of-view and greater resolution.

Chapter 6

Conclusion

The main goal of this thesis was to develop a UV excitation PARS system capable of producing images of cell nuclei within cell cultures and tissue samples. This was achieved in our first iteration, where a parabolic focusing element was used along with mechanical stage scanning to obtain images of a sectioned HT1080 CAM tumor, where cell nuclei were observable. However, the resolution of this system, determined to be 0.70-µm, could be improved and mechanical stage scanning resulted in slow acquisition times. The second iteration of the system used a reflective objective, along with galvanometer optical scanning, and was able to clearly image cell nuclei in a variety of tissue samples with a quantified resolution of 0.39-µm. A higher NA also resulted in a tighter DOF, which we demonstrated could provide superficial optical sectioning within tissue samples, allowing the visualization of single cell layers whilst rejecting background signal from other layers. Additionally, observations of cells undergoing mitosis also illustrated the range of potential applications this technique could be applied to in the field of biology. The last work presented conducted preliminary work on focusing prior to optical scanning in order to move our system towards fast widefield imaging, an important goal for eventual intraoperative translation of UV-PARS. In light of the current lack of intraoperative techniques for evaluating tumor resection margins, the work presented in this thesis demonstrates real potential to develop into a solution that could solve this significant problem.

Future work will involve moving towards imaging resected tumor tissue in collaboration with pathologists to determine if our system is capable of visualizing resection margins. Depending on the success of optical-sectioning capable architectures currently only verified via simulations, that is coherence-

gated PARS (CG-PARS) [73] and interferometric quadrature PARS (iQ-PARS) [74], with greater optical sectioning capability, 3D UV-PARS images of thicker tissues could be possible. As of now, Yao et al. determined a depth characterization of 100-µm *in vivo* using their UV-PAM system [54], with similar performance this could allow us to image "bread-loafed" tissue sections directly, while still maintaining higher surface sampling than conventional FFPE H&E histology or FSA. Decreasing acquisition times sufficiently will involve moving towards a UV-PARS system with fast optical scanning, which could be achieved by using resonant MEMS or polygon scanning mirrors along with development of a higher pulse repetition rate 266-nm source. Taken with mosaic scanning, this could provide the sampling rate capability required for clinical translation in an intraoperative setting. More work will also have to be done on imaging un-sectioned tissue, where surface irregularities are accounted for, or tissue surfaces are flattened prior to imaging. Further down the road, miniaturization of the scan-head, using MEMS scanning mirrors, could also eventually lead to a fiber-tethered probe that allows for resection bed scanning.

In order to increase imaging specificity, especially in the case of fresh tissue imaging, where minimally washed resection samples could still contain significant quantities of residual blood contamination, future work will require multi-wavelength illumination to decouple signal contributions from different biomolecules, for example, introducing 532-nm excitation to detect oxy- and/or deoxy- hemoglobin contrast. Since conventional H&E histology stains both the nucleus and surrounding cytoplasm, further work should also look towards investigating other wavelengths in order to obtain cytoplasm contrast, for an eosin equivalent virtual stain. Furthermore, exploring lipid contrast by, for example, using 1210-nm wavelength excitation [75], could also provide valuable information that is currently available in certain NLM modalities.

In terms of widefield imaging, when focusing prior to scanning, light deflected away from the optical axis inherently has to travel further to reach the sample surface. This becomes more noticeable as the NA of the system increases,

since the DOF becomes tighter. As a result, future work should look into integrating fast translation of the objective, via for example an objective scanner, to allow for higher resolution widefield imaging.

As of yet, similar to UV-PAM, our laser fluences are currently above MPE limits for the skin of human subjects [54]. As of yet, the main applications of this technology are for cell imaging and *ex vivo* tissue imaging where MPE limits do not apply. However, subsequent work should aim to further reduce laser exposure to mitigate potential tissue damage for future applications that will involve *in vivo* work.

Bibliography

1. F. T. Nguyen, A. M. Zysk, E. J. Chaney, J. G. Kotynek, U. J. Oliphant, F. J. Bellafiore, K. M. Rowland, P. A. Johnson, and S. A. Boppart, "Intraoperative evaluation of breast tumor margins with optical coherence tomography," Cancer Res. **69,** 8790-8796 (2009).

2. S. Abeytunge, Y. Li, B. A. Larson, G. Peterson, E. Seltzer, R. Toledo-Crow, and M. Rajadhyaksha, "Confocal microscopy with strip mosaicing for rapid imaging over large areas of excised tissue," J. Biomed. Opt. **18,** 061227 (2013).

3. H. Tu, Y. Liu, D. Turchinovich, M. Marjanovic, J. K. Lyngsø, J. Lægsgaard, E. J. Chaney, Y. Zhao, S. You, and W. L. Wilson, "Stain-free histopathology by programmable supercontinuum pulses," Nature photonics **10,** 534 (2016).

4. Y. Chen, W. Xie, A. K. Glaser, N. P. Reder, C. Mao, S. M. Dintzis, J. C. Vaughan, and J. T. Liu, "Rapid pathology of lumpectomy margins with open-top light-sheet (OTLS) microscopy," Biomedical optics express **10,** 1257-1272 (2019).

5. M. Jermyn, K. Mok, J. Mercier, J. Desroches, J. Pichette, K. Saint-Arnaud, L. Bernstein, M. Guiot, K. Petrecca, and F. Leblond, "Intraoperative brain cancer detection with Raman spectroscopy in humans," Science translational medicine **7,** 274ra19 (2015).

6. M. Wang, D. B. Tulman, A. B. Sholl, S. H. Mandava, M. M. Maddox, B. R. Lee, and J. Quincy Brown, "Partial nephrectomy margin imaging using structured illumination microscopy," Journal of biophotonics **11,** e201600328 (2018).

7. A. Graham Bell, "On the production and reproduction of sound by light," 305-324 (1880).

8. I. G. Calasso, W. Craig, and G. J. Diebold, "Photoacoustic point source," Phys. Rev. Lett. **86,** 3550 (2001).

9. L. V. Wang, "Tutorial on photoacoustic microscopy and computed tomography," IEEE Journal of Selected Topics in Quantum Electronics **14,** 171-179 (2008).

10. M. Xu and L. V. Wang, "Photoacoustic imaging in biomedicine," Rev. Sci. Instrum. **77,** 041101 (2006).

11. P. Beard, "Biomedical photoacoustic imaging," Interface focus **1,** 602-631 (2011).

12. L. V. Wang and S. Hu, "Photoacoustic tomography: in vivo imaging from organelles to organs," Science **335,** 1458-1462 (2012).

13. L. V. Wang, "Multiscale photoacoustic microscopy and computed tomography," Nature photonics **3,** 503 (2009).

14. H. F. Zhang, K. Maslov, G. Stoica, and L. V. Wang, "Functional photoacoustic microscopy for high-resolution and noninvasive in vivo imaging," Nat. Biotechnol. **24,** 848 (2006).

15. K. Maslov, H. F. Zhang, S. Hu, and L. V. Wang, "Optical-resolution photoacoustic microscopy for in vivo imaging of single capillaries," Opt. Lett. **33,** 929-931 (2008).

16. J. Yao and L. V. Wang, "Photoacoustic microscopy," Laser & photonics reviews **7,** 758-778 (2013).

17. C. Zhang, K. Maslov, and L. V. Wang, "Subwavelength-resolution label-free photoacoustic microscopy of optical absorption in vivo," Opt. Lett. **35,** 3195-3197 (2010).

18. L. V. Wang and H. Wu, *Biomedical optics: principles and imaging* (John Wiley & Sons, 2012).

19. P. Hajireza, W. Shi, K. Bell, R. J. Paproski, and R. J. Zemp, "Non-interferometric photoacoustic remote sensing microscopy," Light: Science & Applications **6,** e16278 (2017).

20. K. L. Bell, P. H. Reza, and R. J. Zemp, "Real-time functional photoacoustic remote sensing microscopy," Opt. Lett. **44,** 3466-3469 (2019).

21. P. H. Reza, K. Bell, W. Shi, J. Shapiro, and R. J. Zemp, "Deep non-contact photoacoustic initial pressure imaging," Optica **5,** 814-820 (2018).

22. L. Huo, "A practical approach to grossing breast specimens," Ann. Diagn. Pathol. **15,** 291-301 (2011).

23. F. Fereidouni, Z. T. Harmany, M. Tian, A. Todd, J. A. Kintner, J. D. McPherson, A. D. Borowsky, J. Bishop, M. Lechpammer, and S. G. Demos, "Microscopy with ultraviolet surface excitation for rapid slide-free histology," Nature biomedical engineering **1,** 957 (2017).

24. B. E. Bejnordi, G. Litjens, N. Timofeeva, I. Otte-Höller, A. Homeyer, N. Karssemeijer, and van der Laak, Jeroen AWM, "Stain specific standardization of whole-slide histopathological images," IEEE Trans. Med. Imaging **35,** 404-415 (2015).

25. R. J. Buesa, "Histology: a unique area of the medical laboratory," Ann. Diagn. Pathol. **11,** 137-141 (2007).

26. J. M. Eschbacher, J. F. Georges, E. Belykh, M. I. Yazdanabadi, N. L. Martirosyan, E. Szeto, C. Y. Seiler, M. A. Mooney, J. K. Daniels, and K. Y. Goehring, "Immediate label-free ex vivo evaluation of human brain tumor biopsies with confocal reflectance microscopy," Journal of Neuropathology & Experimental Neurology **76,** 1008-1022 (2017).

27. L. S. Eberlin, R. J. Tibshirani, J. Zhang, T. A. Longacre, G. J. Berry, D. B. Bingham, J. A. Norton, R. N. Zare, and G. A. Poultsides, "Molecular assessment of surgical-resection margins of gastric cancer by mass-spectrometric imaging," Proceedings of the National Academy of Sciences **111,** 2436-2441 (2014).

28. S. A. McLaughlin, L. M. Ochoa-Frongia, S. M. Patil, H. S. Cody III, and L. M. Sclafani, "Influence of frozen-section analysis of sentinel lymph node and lumpectomy margin status on reoperation rates in patients undergoing breast-conservation therapy," J. Am. Coll. Surg. **206,** 76-82 (2008).

29. V. Rastogi, N. Puri, S. Arora, G. Kaur, L. Yadav, and R. Sharma, "Artefacts: a diagnostic dilemma–a review," Journal of clinical and diagnostic research: JCDR **7,** 2408 (2013).

30. A. K. Glaser, N. P. Reder, Y. Chen, E. F. McCarty, C. Yin, L. Wei, Y. Wang, L. D. True, and J. T. Liu, "Light-sheet microscopy for slide-free non-destructive pathology of large clinical specimens," Nature biomedical engineering **1,** 0084 (2017).

31. C. E. Cox, N. N. Ku, D. S. Reintgen, H. M. Greenberg, S. V. Nicosia, and S. Wangensteen, "Touch preparation cytology of breast lumpectomy margins with histologic correlation," Archives of Surgery **126,** 490-493 (1991).

32. Y. Li, R. Rey-Dios, D. W. Roberts, P. A. Valdés, and A. A. Cohen-Gadol, "Intraoperative fluorescence-guided resection of high-grade gliomas: a

comparison of the present techniques and evolution of future strategies," World neurosurgery **82,** 175-185 (2014).

33. T. Karni, I. Pappo, J. Sandbank, O. Lavon, V. Kent, R. Spector, S. Morgenstern, and S. Lelcuk, "A device for real-time, intraoperative margin assessment in breast-conservation surgery," The American Journal of Surgery **194,** 467-473 (2007).

34. L. L. De Boer, B. G. Molenkamp, T. M. Bydlon, B. Hendriks, J. Wesseling, H. Sterenborg, and T. J. Ruers, "Fat/water ratios measured with diffuse reflectance spectroscopy to detect breast tumor boundaries," Breast Cancer Res. Treat. **152,** 509-518 (2015).

35. O. Olsha, D. Shemesh, M. Carmon, O. Sibirsky, R. A. Dalo, L. Rivkin, and I. Ashkenazi, "Resection margins in ultrasound-guided breast-conserving surgery," Annals of surgical oncology **18,** 447-452 (2011).

36. Y. B. Ji, S. J. Oh, S. Kang, J. Heo, S. Kim, Y. Choi, S. Song, H. Y. Son, S. H. Kim, and J. H. Lee, "Terahertz reflectometry imaging for low and high grade gliomas," Scientific reports **6,** 36040 (2016).

37. R. Tang, J. M. Buckley, L. Fernandez, S. Coopey, O. Aftreth, J. Michaelson, M. Saksena, L. Lei, M. Specht, and M. Gadd, "Micro-computed tomography (Micro-CT): a novel approach for intraoperative breast cancer specimen imaging," Breast Cancer Res. Treat. **139,** 311-316 (2013).

38. C. Senft, A. Bink, K. Franz, H. Vatter, T. Gasser, and V. Seifert, "Intraoperative MRI guidance and extent of resection in glioma surgery: a randomised, controlled trial," The lancet oncology **12,** 997-1003 (2011).

39. C. J. Mann, L. Yu, C. Lo, and M. K. Kim, "High-resolution quantitative phase-contrast microscopy by digital holography," Optics Express **13,** 8693-8698 (2005).

40. W. Xie, Y. Chen, Y. Wang, L. Wei, C. Yin, A. K. Glaser, M. E. Fauver, E. J. Seibel, S. M. Dintzis, and J. C. Vaughan, "Microscopy with ultraviolet surface excitation for wide-area pathology of breast surgical margins," J. Biomed. Opt. **24,** 026501 (2019).

41. D. Huang, E. A. Swanson, C. P. Lin, J. S. Schuman, W. G. Stinson, W. Chang, M. R. Hee, T. Flotte, K. Gregory, and C. A. Puliafito, "Optical coherence tomography," Science **254,** 1178-1181 (1991).

42. S. J. Erickson-Bhatt, R. M. Nolan, N. D. Shemonski, S. G. Adie, J. Putney, D. Darga, D. T. McCormick, A. J. Cittadine, A. M. Zysk, and M. Marjanovic, "Real-time imaging of the resection bed using a handheld probe to reduce incidence of microscopic positive margins in cancer surgery," Cancer Res. **75,** 3706-3712 (2015).

43. J. Pawley, *Handbook of biological confocal microscopy* (Springer Science & Business Media, 2010).

44. M. Ragazzi, S. Piana, C. Longo, F. Castagnetti, M. Foroni, G. Ferrari, G. Gardini, and G. Pellacani, "Fluorescence confocal microscopy for pathologists," Modern Pathology **27,** 460 (2014).

45. P. Friedl, K. Wolf, G. Harms, and U. H. von Andrian, "Biological second and third harmonic generation microscopy," Current Protocols in Cell Biology **34,** 4.15.-4.15. 21 (2007).

46. J. Cheng and X. S. Xie, "Coherent Anti-Stokes Raman Scattering Microscopy: Instrumentation, Theory, and Applications," The Journal of Physical Chemistry B827-840 (2004).

47. N. Dudovich, D. Oron, and Y. Silberberg, "Single-pulse coherently controlled nonlinear Raman spectroscopy and microscopy," Nature **418,** 512 (2002).

48. C. W. Freudiger, W. Min, B. G. Saar, S. Lu, G. R. Holtom, C. He, J. C. Tsai, J. X. Kang, and X. S. Xie, "Label-free biomedical imaging with high sensitivity by stimulated Raman scattering microscopy," Science **322,** 1857-1861 (2008).

49. S. You, H. Tu, E. J. Chaney, Y. Sun, Y. Zhao, A. J. Bower, Y. Liu, M. Marjanovic, S. Sinha, and Y. Pu, "Intravital imaging by simultaneous label-free autofluorescence-multiharmonic microscopy," Nature communications **9,** 2125 (2018).

50. M. Wang, D. B. Tulman, A. B. Sholl, H. Z. Kimbrell, S. H. Mandava, K. N. Elfer, S. Luethy, M. M. Maddox, W. Lai, and B. R. Lee, "Gigapixel surface imaging of radical prostatectomy specimens for comprehensive detection of cancer-positive surgical margins using structured illumination microscopy," Scientific reports **6,** 27419 (2016).

51. H. L. Fu, J. L. Mueller, M. P. Javid, J. K. Mito, D. G. Kirsch, N. Ramanujam, and J. Q. Brown, "Optimization of a widefield structured illumination microscope for non-destructive assessment and quantification of nuclear features in tumor margins of a primary mouse model of sarcoma," PloS one **8,** e68868 (2013).

52. J. Mertz, "Optical sectioning microscopy with planar or structured illumination," Nature methods **8,** 811 (2011).

53. D. Yao, K. I. Maslov, L. V. Wang, R. Chen, and Q. Zhou, "Optimal ultraviolet wavelength for in vivo photoacoustic imaging of cell nuclei," J. Biomed. Opt. **17,** 056004 (2012).

54. D. Yao, K. Maslov, K. K. Shung, Q. Zhou, and L. V. Wang, "In vivo label-free photoacoustic microscopy of cell nuclei by excitation of DNA and RNA," Opt. Lett. **35,** 4139-4141 (2010).

55. T. T. Wong, R. Zhang, P. Hai, C. Zhang, M. A. Pleitez, R. L. Aft, D. V. Novack, and L. V. Wang, "Fast label-free multilayered histology-like imaging of human breast cancer by photoacoustic microscopy," Science advances **3,** e1602168 (2017).

56. D. Cai, T. T. Wong, L. Zhu, J. Shi, S. Chen, and L. V. Wang, "Dual-view photoacoustic microscopy for quantitative cell nuclear imaging," Opt. Lett. **43,** 4875-4878 (2018).

57. X. Liu, T. T. Wong, J. Shi, J. Ma, Q. Yang, and L. V. Wang, "Label-free cell nuclear imaging by Grüneisen relaxation photoacoustic microscopy," Opt. Lett. **43,** 947-950 (2018).

58. T. Imai, J. Shi, T. T. Wong, L. Li, L. Zhu, and L. V. Wang, "High-throughput ultraviolet photoacoustic microscopy with multifocal excitation," J. Biomed. Opt. **23,** 036007 (2018).

59. B. E. Bejnordi, N. Timofeeva, I. Otte-Höller, N. Karssemeijer, and van der Laak, Jeroen AWM, "Quantitative analysis of stain variability in histology slides and an algorithm for standardization," in *Medical Imaging 2014: Digital Pathology,* Anonymous (International Society for Optics and Photonics, 2014), pp. 904108.

60. T. T. Wong, R. Zhang, C. Zhang, H. Hsu, K. I. Maslov, L. Wang, J. Shi, R. Chen, K. K. Shung, and Q. Zhou, "Label-free automated three-dimensional imaging of whole organs by microtomy-assisted photoacoustic microscopy," Nature communications **8,** 1386 (2017).

61. Y. K. Tao, D. Shen, Y. Sheikine, O. O. Ahsen, H. H. Wang, D. B. Schmolze, N. B. Johnson, J. S. Brooker, A. E. Cable, and J. L. Connolly, "Assessment of breast pathologies using nonlinear microscopy," Proceedings of the National Academy of Sciences **111,** 15304-15309 (2014).

62. M. Ji, S. Lewis, S. Camelo-Piragua, S. H. Ramkissoon, M. Snuderl, S. Venneti, A. Fisher-Hubbard, M. Garrard, D. Fu, and A. C. Wang, "Detection of human brain tumor infiltration with quantitative stimulated Raman scattering microscopy," Science translational medicine **7,** 309ra163 (2015).

63. O. M. Carrasco-Zevallos, C. Viehland, B. Keller, M. Draelos, A. N. Kuo, C. A. Toth, and J. A. Izatt, "Review of intraoperative optical coherence tomography: technology and applications," Biomedical optics express **8,** 1607-1637 (2017).

64. O. Uckermann, R. Galli, S. Tamosaityte, E. Leipnitz, K. D. Geiger, G. Schackert, E. Koch, G. Steiner, and M. Kirsch, "Label-free delineation of brain tumors by coherent anti-stokes Raman scattering microscopy in an orthotopic mouse model and human glioblastoma," PLoS One **9,** e107115 (2014).

65. D. S. Gareau, H. Jeon, K. S. Nehal, and M. Rajadhyaksha, "Rapid screening of cancer margins in tissue with multimodal confocal microscopy," J. Surg. Res. **178,** 533-538 (2012).

66. K. Bell, P. Hajireza, and R. Zemp, "Scattering cross-sectional modulation in photoacoustic remote sensing microscopy," Opt. Lett. **43,** 146-149 (2018).

67. K. L. Bell, P. Hajireza, W. Shi, and R. J. Zemp, "Temporal evolution of low-coherence reflectrometry signals in photoacoustic remote sensing microscopy," Appl. Opt. **56,** 5172-5181 (2017).

68. M. Schürmann, J. Scholze, P. Müller, J. Guck, and C. J. Chan, "Cell nuclei have lower refractive index and mass density than cytoplasm," Journal of biophotonics **9,** 1068-1076 (2016).

69. Eksma Optics, "Crystals," .

70. T. C. Hollon, S. Lewis, B. Pandian, Y. S. Niknafs, M. R. Garrard, H. Garton, C. O. Maher, K. McFadden, M. Snuderl, and A. P. Lieberman, "Rapid intraoperative diagnosis of pediatric brain tumors using stimulated Raman histology," Cancer Res. **78,** 278-289 (2018).

71. N. J. Haven, K. L. Bell, P. Kedarisetti, J. D. Lewis, and R. J. Zemp, "Ultraviolet photoacoustic remote sensing microscopy," Opt. Lett. **44,** 3586-3589 (2019).

72. A. F. Frangi, W. J. Niessen, K. L. Vincken, and M. A. Viergever, "Multiscale vessel enhancement filtering," in *International conference on medical image computing and computer-assisted intervention,* Anonymous (Springer, 1998), pp. 130-137.

73. K. L. Bell, P. Hajireza, and R. J. Zemp, "Coherence-gated photoacoustic remote sensing microscopy," Optics express **26,** 23689-23704 (2018).

74. M. T. Martell, K. L. Bell, and R. J. Zemp, "Optical absorption coherence tomography (OACT) with interferometric quadrature photoacoustic remote sensing (iQ-PARS)" in *SPIE ECBO*.

75. C. Tsai, J. Chen, and W. Wang, "Near-infrared absorption property of biological soft tissue constituents," Journal of Medical and Biological Engineering **21,** 7-14 (2001).